BACH family members regulate angiogenesis and lymphangiogenesis by modulating VEGFC expression

Batya Cohen[1], Hanoch Tempelhof[1], Tal Raz[2], Roni Oren[1] Julian Nicenboim[1], Filip Bochner[1], Ron Even[1], Adam Jelinski[1], Raya Eilam[3], Shifra Ben-Dor[4], Yoseph Adaddi[4], Ofra Golani[4], Shlomi Lazar[5], Karina Yaniv[1*] and Michal Neeman[1*]

[1]Department of Biological Regulation, Weizmann Institute of Science, Rehovot 76100, Israel. [2]Koret School of Veterinary Medicine, The Hebrew University of Jerusalem, Rehovot, 76100 Israel. [3]Department of Veterinary Resources, Weizmann Institute of Science, Rehovot 76100, Israel. [4]Life Sciences Core Facilities, Weizmann Institute of Science, Rehovot 76100, Israel. [5]Department of Pharmacology, Israel Institute for Biological Research, Ness-Ziona 74100, Israel.
* Corresponding authors

Abstract

Angiogenesis and lymphangiogenesis are key processes during embryogenesis as well as under physiological and pathological conditions. Vascular endothelial growth factor C (VEGFC), the ligand for both VEGFR2 and VEGFR3, is a central lymphangiogenic regulator that also drives angiogenesis. Here we report that members of the highly conserved BACH (BTB and CNC homology) family of transcription factors regulate VEGFC expression, through direct binding to its promoter. Accordingly, downregulation of *bach2a* hinders blood-vessel formation and impairs lymphatic sprouting in a *vegfc*-dependent manner during zebrafish embryonic development. In contrast, BACH1-overexpression enhances intratumoral blood-vessel density and peritumoral lymphatic vessel diameter in ovarian and lung mouse tumor models. The effects on the vascular compartment correlate spatially and temporally with BACH1 transcriptional regulation of *VEGFC* expression. Altogether, our results uncover a novel role for the BACH/VEGFC signaling axis in lymphatic formation during embryogenesis and cancer, providing a novel potential target for therapeutic interventions.

Introduction

The blood and lymphatic networks are two evolutionarily conserved transport systems that provide complementary functions in the maintenance of tissue homeostasis. In particular, the formation of new blood and lymphatic vessels is a prerequisite for vertebrate embryonic and postnatal development. During embryogenesis, the blood circulatory system is first to emerge. As early as mouse embryonic day (E) 7.5, vasculogenesis, the formation of a primitive vascular plexus through proliferation, migration and differentiation of endothelial cells (ECs), takes place. Later on, this plexus undergoes massive remodeling via angiogenesis, which involves also arterio-venous differentiation (A. S. Chung & Ferrara, 2011). At E10.5, a distinct subpopulation of ECs within the cardinal vein commits to the lymphatic lineage, buds off and migrates to establish primitive lymph sacs, which through further sprouting give rise to the peripheral lymphatic system (Oliver & Alitalo, 2005; Semo, Nicenboim, & Yaniv, 2016). During adult life, the majority of blood and lymphatic vessels are quiescent, with the exception of female reproductive organs during the ovarian cycle and the placenta during pregnancy. Reactivation of angiogenesis and lymphangiogenesis, however, is a hallmark of pathological processes associated with wound healing, myocardial infarction (MI), allograft rejection, chronic inflammation, tumor progression and malignant cell dissemination (A. S. Chung & Ferrara, 2011; Oliver & Alitalo, 2005).

The VEGF family of growth factors and its receptors are central signaling pathways, controlling angiogenesis and lymphangiogenesis during development and adulthood. VEGFs exert their activity by binding to the tyrosine kinase receptors (vascular endothelial growth factor receptor-1) VEGFR-1, VEGFR-2, and VEGFR-3, expressed in blood and lymphatic endothelial cells (LECs) (Lohela, Bry, Tammela, & Alitalo, 2009). VEGFA, the ligand for VEGFR-1 and VEGFR-2, is best known for its role in angiogenesis, stimulating EC proliferation and migration and increasing vascular permeability. VEGFB, which also binds to VEGFR1, plays a role in cell survival and indirectly promotes VEGFA induced angiogenesis (Lal, Puri, & Rodrigues, 2018).

VEGFC is another critical player in VEGF signaling. This protein, which signals through the receptors VEGFR-3 and VEGFR-2, plays a key role across species, guiding both lymphatic and blood vasculature development and remodeling (Gore et al., 2011; Hogan, Bos, et al., 2009; Karkkainen et al., 2004; Kuchler et al., 2006; Lohela et al., 2009; Shin et al., 2016; Villefranc et al., 2013; Yaniv et al., 2006). VEGFC is expressed by endothelial and non-

endothelial cells, thus acting via both autocrine and paracrine signaling (Covassin, Villefranc, Kacergis, Weinstein, & Lawson, 2006; Helker et al., 2013; Khromova, Kopnin, Rybko, & Kopnin, 2012; Kodama et al., 2008; Lohela, Helotera, Haiko, Dumont, & Alitalo, 2008; Villefranc et al., 2013). Evidence for its necessity for proper lymph formation is revealed by the finding that ectopic expression of VEGFC in mouse ear or skin keratinocytes results in hyperplasia of lymphatic vessels. Similarly, mice and zebrafish lacking VEGFC fail to develop a lymphatic vasculature as initial sprouting and directed migration of lymphatic progenitors from the cardinal vein are arrested (Karkkainen et al., 2004; Kuchler et al., 2006; Shin et al., 2016; Villefranc et al., 2013; Yaniv et al., 2006). In addition to its predominant role in lymphangiogenesis, VEGFC was shown to induce angiogenesis upon overexpression in the mouse cornea, skin or ischemic hindlimb. Moreover, coronary vessel development is VEGFC dependent, and hearts devoid of VEGFC reveal dramatic delay in the formation of subepicardial sprouts (H. I. Chen et al., 2014). Recently, it has been shown by *in vitro* studies that the let-7a/TGFBR3 axis regulates angiogenesis through transcriptional regulation of *VEGFC* (Wang et al., 2019).

VEGFC has a critical role not only during development but also during tumor progression. In various human cancers, enhanced expression of VEGFC and higher levels of VEGFC in serum are commonly associated with tumor aggressiveness and lymph-node metastasis (Lohela et al., 2009; Su et al., 2007). In esophageal carcinoma, for instance, angiogenesis is driven via the phosphoinositide-phospholipase C-ε (PI-PLCε)/NF-κB signaling pathway by direct promotion of *VEGFC* transcription (Y. Chen et al., 2019). In xenograft or transgenic tumor models, stimulation of lymphangiogenesis by VEGFC promotes malignant cell dissemination (Stacker et al., 2014). Furthermore, blockade of *VEGFC* expression in tumor cells by stably transfected small interfering RNAs reduces lymphangiogenesis and lymph node metastasis of murine mammary cancers. Similarly, soluble VEGFR-3 protein has been shown to inhibit VEGFC-induced tumor lymphangiogenesis and metastatic spread in a breast cancer mouse model (Wissmann & Detmar, 2006).

A series of environmental and cellular factors were shown to modulate VEGFC expression. For instance, Interleukin-6 (IL-6) and interleukin-17 (IL-17) regulate VEGFC expression via the PI3K-Akt or ERK 1/2 pathways, whereas MicroRNA-1826 significantly down-regulates VEGFC expression in human bladder cancer (J. C. Chen, Chang, Hong, Yu, & Su, 2012). *Vegfc* mRNA levels are heightened in the adipose tissue of obese mice, pointing to

adipocytes as a source of elevated VEGFC levels in obesity (Karaman et al., 2015). In adults, inflammation induces robust upregulation of VEGFC expression by macrophages (Baluk et al., 2005). Additionally, various hormones, transcription factors, metallothioneins and microenvironmental stresses (e.g., hyperthermia, oxidative stress, high salt) were shown to control VEGFC expression (J. C. Chen et al., 2012; Cohen et al., 2009; Gauvrit et al., 2018; Machnik et al., 2009; Sapoznik et al., 2009; Schuermann, Helker, & Herzog, 2015).

Here, we report that BACH transcription factors, which are known to be involved in various intracellular signaling pathways, modulate VEGFC expression during embryonic development and tumor progression, offering a better understanding of blood and lymph vessel formation during physiological and pathological conditions.

Results

Spatial and temporal expression of *bach2* during zebrafish development

In order to explore the molecular mechanisms governing VEGFC expression, we searched for genes that co-express with *VEGFC* in human prostate cancer datasets (Glinsky, Glinskii, Stephenson, Hoffman, & Gerald, 2004). We identified 434 genes, on which we further applied the Promoters of Clusters (POC) analysis (Tabach et al., 2007). This method screens the promoters of genes with shared biological function against a library of transcription factor binding motifs and identifies those which are statistically over-represented. Five factors passed the basic significance threshold, out of which only two possessed binding sites within the *VEGFC* promoter. We then searched for evolutionarily conserved regions, which often represent potential DNA regulatory elements (Ovcharenko, Nobrega, Loots, & Stubbs, 2004). Comparison of the *VEGFC* promoters of human, mouse and zebrafish revealed two highly conserved BACH (BTB and CNC homology) binding sequences (Figure 1A).

The BACH family of transcription factors comprises two members, BACH1 and BACH2. In mammals, BACH1 is expressed ubiquitously and has been shown to act either as an activator or repressor of transcription and to be involved in oxidative stress, metabolism, cell transformation, neurodegenerative diseases, tumor expansion and metastatic spread (Igarashi & Watanabe-Matsui, 2014; J. Lee et al., 2014; J. Lee et al., 2019; Lignitto et al., 2019; Nakanome et al., 2013; Warnatz et al., 2011; Watari et al., 2008; Wiel et al., 2019; Zhou, Wu, Zhao, Chang, & Lu, 2016). BACH2 is a transcriptional repressor crucial for the terminal differentiation and maturation of both T and B lymphocytes (Sidwell & Kallies, 2016) and

its loss is associated with severe autoimmune diseases. BACH proteins are highly conserved in vertebrates, particularly in the functional (BTB and bZip) domains and the regions immediately surrounding them (Igarashi & Watanabe-Matsui, 2014). Zebrafish have four *bach* genes with homology to mammalian BACH: *bach1a*, *bach1b*, *bach2a* and *bach2b* (Fuse, Nakajima, Nakajima-Takagi, Nakajima, & Kobayashi, 2015; Luo et al., 2016; Zhang et al., 2014).

As a first step, we evaluated the expression pattern of the different *bach* transcripts in ECs isolated by Fluorescence-Activated Cell Sorting (FACS) from *Tg(fli1:EGFP)*^{y1} (Lawson & Weinstein, 2002) zebrafish embryos (L. Covassin et al., 2006). We found the transcripts of *bach2a* and *bach2b* to be more abundant than *bach1b*, while *bach1a* is barely detectable in the GFP-positive (GFP^{+}) cell population, at either 21-24 hours post-fertilization (hpf) or 3 days post fertilization (dpf) (Figure 1B). Consequently, we focused our studies on *bach2a* and *bach2b,* as they are the major paralogs expressed in the endothelium. To assess the spatial and temporal expression patterns of *bach2a* and *bach2b* during zebrafish embryogenesis, we performed whole-mount *in situ* hybridization (WISH). Abundant expression of *bach2a* and *bach2b* was apparent in the somites and somite boundaries at 20 hpf and up to 48 hpf (Figure 1C). Furthermore, we detected strong enrichment of *bach2a* transcripts in myotomes and in several areas of the central nervous system (CNS), including the hindbrain, midbrain-hindbrain boundary, midbrain and forebrain (Figure 1- figure supplement 1).

Figure 1

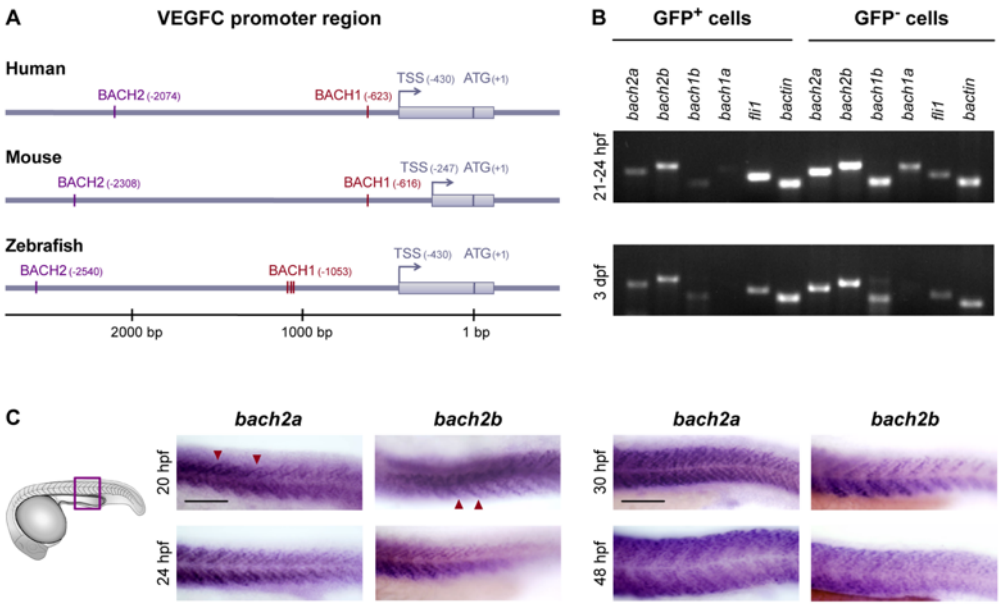

Spatial and temporal expression of *bach2* paralog transcripts during zebrafish development.

(A) BACH putative binding sites are evolutionary conserved in the VEGFC promoter region. Numbering is from the ATG (translation initiation) due to the difference in length of the mouse's 5' UTR. An arrow indicates Transcription Start Site (TSS), and the location of the first exon is marked as a gray rectangle. The location of the BACH sites is as predicted by Genomatix Genome Analyzer MatInspector: Human (NM_005429.4 TSS at hg19, chr4:177713899 on the minus strand); Mouse (NM_009506.2 TSS at mm9, chr8:54077532 on the plus strand); Zebrafish (NM_205734.1 TSS at Zv9, chr1:39270725 on the minus strand). **(B)** Semi-quantitative RT-PCR analysis of the indicated genes in enriched GFP^+ cells isolated by FACS from *Tg(fli1:EGFP)*^{y1} embryos at two developmental time points, 21-24 hpf and 3 dpf (two independent experiments for each time point). **(C)** A lateral view of the trunk region of a wild-type zebrafish embryo at 20, 24, 30 and 48 hpf, detected with a specific *bach2a* or *bach2b* anti-sense mRNA probe. A red arrowhead indicates somite boundaries. Scale bar, 100 µm.

Figure 1- figure supplement 1

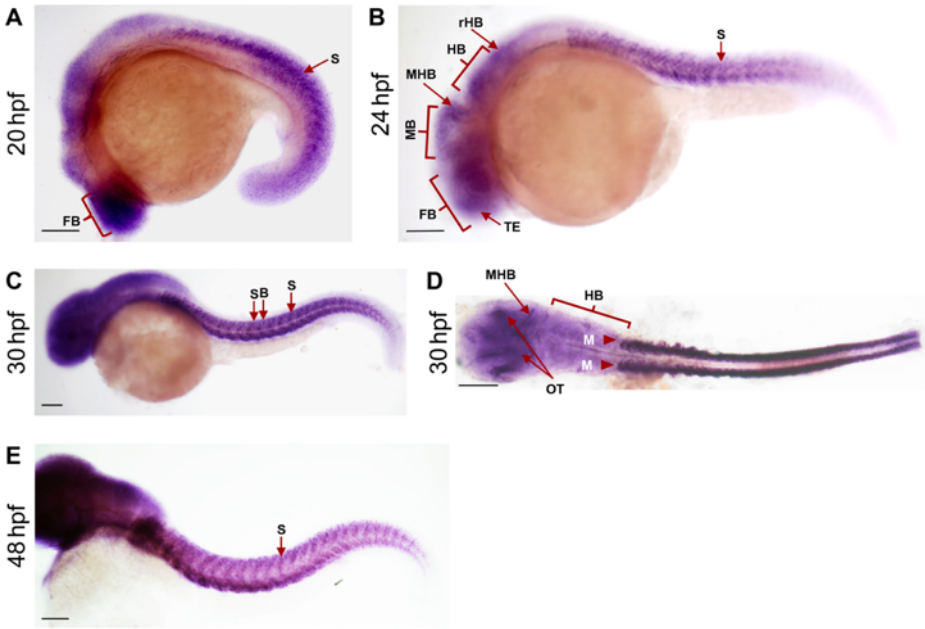

Expression of *bach2a* at different stages during zebrafish development.

Embryos at 20 **(A)**, 24 **(B)**, 30 **(C, D)** and 48 **(E)** hpf were examined by whole-mount *in situ* hybridization with an antisense *bach2a* riboprobe. Abbreviations: FB, forebrain; S, somite; TE, telencephalon; MB, midbrain; MHB, midbrain hindbrain boundary; HB, hindbrain; rHB, rostral hindbrain; SB, somite-boundaries; M, myotomes; OT, optic tectum. Scale bar, 500 µm.

bach2a is essential for developmental angiogenesis and lymphangiogenesis

We then assessed the contribution of BACH to angiogenesis and lymphangiogenesis during embryonic development and, specifically, investigated their putative role as regulators of *vegfc* expression and function during zebrafish vasculature formation. We used antisense morpholino oligonucleotides (MOs) to knockdown the expression of the two *bach2* paralogs and then surveyed the phenotypic changes at different stages of development. At 30 hpf, clear defects were observed in the primordial hindbrain channel (PHBC) in *bach2a* MO-

injected *Tg(fli1:EGFP)*^{y1} zebrafish embryos (Figures 2A and 2B). Similar phenotypes were detected in *vegfc* morphants (Figures 2A and 2B), in line with previous reports demonstrating impaired PHBC formation following the blocking of Vegfc-activated Vegfr3 signaling (L. D. Covassin et al., 2006; Hogan, Herpers, et al., 2009; Schuermann et al., 2015; Shin et al., 2016; Villefranc et al., 2013). In contrast to *bach2a* downregulation, no defects were detected in *Tg(fli1:EGFP)*^{y1} embryos either injected with different concentrations of *bach2b* MOs (up to 10 ng per embryo, Figures 2A and 2C) or subjected to a *bach2b* CRISPR guide RNA (*bach2b* gRNA, Figure 2- figure supplement 1A, 1B, Figure 2A and 2B). The vascular abnormalities detected upon *bach2a* and *vegfc* knockdown were accompanied by pericardial and body edema, as well as reduced blood flow (Figure 2- figure supplement 2), resembling the phenotypes observed in collagen and calcium-binding EGF domain-1 (*ccbe1*) (Hogan, Bos, et al., 2009) and *vegfc* (Karkkainen et al., 2004; Shin et al., 2016) mutants. In contrast, no morphological abnormalities were observed following *bach2b* knockdown (Figure 2- figure supplement 3A-3C).

To confirm the specificity of the *bach2a* morphant phenotype, we generated *bach2a* mutants using CRISPR/Cas9-mediated gene editing (Figure 2- figure supplement 2C-2E). To our surprise, homozygous *bach2a* mutants displayed no primordial hindbrain channel defects (*bach2a*$^{mut-/-}$, Figures 2D and 2E). We therefore hypothesized that genetic compensation (El-Brolosy et al., 2019; El-Brolosy & Stainier, 2017; Rossi et al., 2015) through activation of *bach2b* could potentially account for the absence of angiogenic phenotypes in *bach2a* mutants. To address this possibility, we mated *bach2a*$^{+/-}$ carriers and injected their progeny with either a sub-dose of *bach2b* MO or with *bach2b* gRNA that does not induce vascular malformations in WT embryos (Figures 2A-2C). Interestingly, PHBC formation defects were identified in ~25% of the embryos, which upon genotyping were found to carry the *bach2a* mutation (*bach2a*$^{mut-/-}$+ *bach2b* MO and *bach2a*$^{mut-/-}$+ *bach2b* gRNA, Figures 2D and 2E), as opposed to their wild-type siblings (*bach2a*$^{mut+/+}$+ *bach2b* MO and *bach2a*$^{mut+/+}$+ *bach2b* gRNA, Figure 2E). Conversely, following *bach2a* MO injection, *bach2a* wild-type siblings displayed PHBC formation defects while homozygous mutants appeared normal (Figures 2D and 2E), suggesting that the *bach2a*$^{mut-/-}$ mutants were less sensitive than their *bach2a*$^{mut+/+}$ siblings to *bach2a* MO injections, and further confirming the specificity of both mutants and morphants. In order to ascertain whether the compensation mechanism involves upregulation of the paralogous *bach2b* gene, we assessed its expression in wild-type and *bach2a* mutants, by RT-qPCR. Surprisingly, while no significant differences in the levels of *bach2b* mRNA

were detected (Figure 2- figure supplement 1F), we observed a slight elevation in *bach2a* mRNA levels in homozygous mutants (Figure 2- figure supplement 1G), suggesting an alternative, yet unknown, mechanism of adaptive compensation following *bach2a* perturbation.

Figure 2

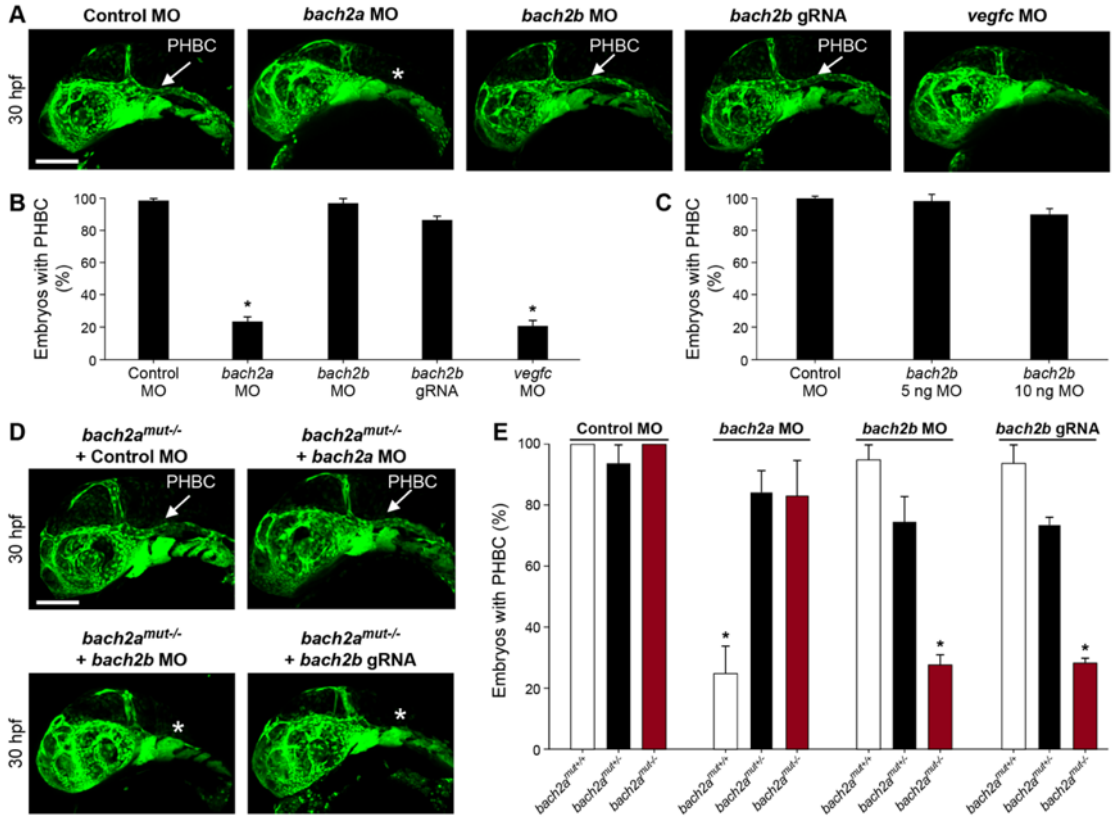

***bach2a* is essential for developmental angiogenesis in zebrafish embryos.**

(A) Confocal images of the primordial hindbrain channel (PHBC, white arrow) of 30-hpf *Tg(fli1:EGFP)*^{y1} embryos injected with control MO (10 ng), *bach2a* MO (3.75 ng), *bach2b* MO (3.75 ng), *bach2b* guide RNA (gRNA,125 ng) or *vegfc* MO (10 ng). Asterisk indicates absence of PHBC. **(B)** Percentage of 30-hpf *Tg(fli1:EGFP)*^{y1} embryos with intact PHBC formation following injection with control MO (10 ng, $n_{\text{Control MO}}$ = 68), *bach2a* MO (3.75 ng, $n_{bach2a\ \text{MO}}$ = 107; **P*<0.0001), *bach2b* MO (3.75 ng, $n_{bach2b\ \text{MO}}$ = 48), *bach2b* guide RNA (gRNA, 125 ng, $n_{bach2b\ \text{gRNA}}$ = 42) or *vegfc* Mo (10 ng, $n_{vegfc\ \text{MO}}$ = 35; **P*<0.0001). Error bars, mean ±s.e.m. **(C)** Percentage of 30-hpf *Tg(fli1:EGFP)*^{y1} embryos with intact PHBC formation following injection with control MO (10 ng, $n_{\text{Control MO}}$ = 24) or an increased concentration of *bach2b* MO (5 ng, $n_{bach2b\ \text{MO 5ng}}$ = 24) or (10 ng, $n_{bach2b\ \text{MO 10ng}}$ = 24). Error bars, mean ± s.e.m.; *P*>0.99999. **(D)** Confocal projection at 30 hpf *Tg(fli1:EGFP)*^{y1} of homozygous *bach2a* mutants (*bach2a*$^{mut-/-}$) from F2 *bach2a*$^{mut+/-}$ incross. White arrow points at an intact PHBC detected in embryos injected with control MO (10 ng, *bach2a*$^{mut-/-}$ + Control MO) and *bach2a* MO (3.75 ng, *bach2a*$^{mut-/-}$ + *bach2a* MO). Asterisk indicates defects in PHBC development following injection with *bach2b* MO (3.75 ng, *bach2a*$^{mut-/-}$ + *bach2b* MO) or *bach2b* gRNA (125 ng, *bach2a*$^{mut-/-}$ + *bach2b* gRNA). Scale bar, 100 µm. **(E)** Percentage of randomly selected *bach2a*$^{+/-}$ F2 incross progeny at 30 hpf with an intact PHBC formation injected with control MO (10 ng, $n_{bach2a\text{mut + Control MO}}$ = 50; *P*>0.99999), *bach2a* MO (3.75 ng, $n_{bach2a\text{mut + }bach2a\ \text{MO}}$ = 75; **P*<0.0002), *bach2b* MO (3.75 ng, $n_{bach2a\text{mut + }bach2a\ \text{MO}}$ = 55; * *P<0.012*) or *bach2b* gRNA (125 ng, $n_{bach2a\text{mut + }bach2b\ \text{gRNA}}$ = 137; * *P*<0.001). Following genotyping, offspring followed the expected Mendelian ratios of inheritance. Error bars, mean ± s.e.m.

Figure 2- figure supplement 1

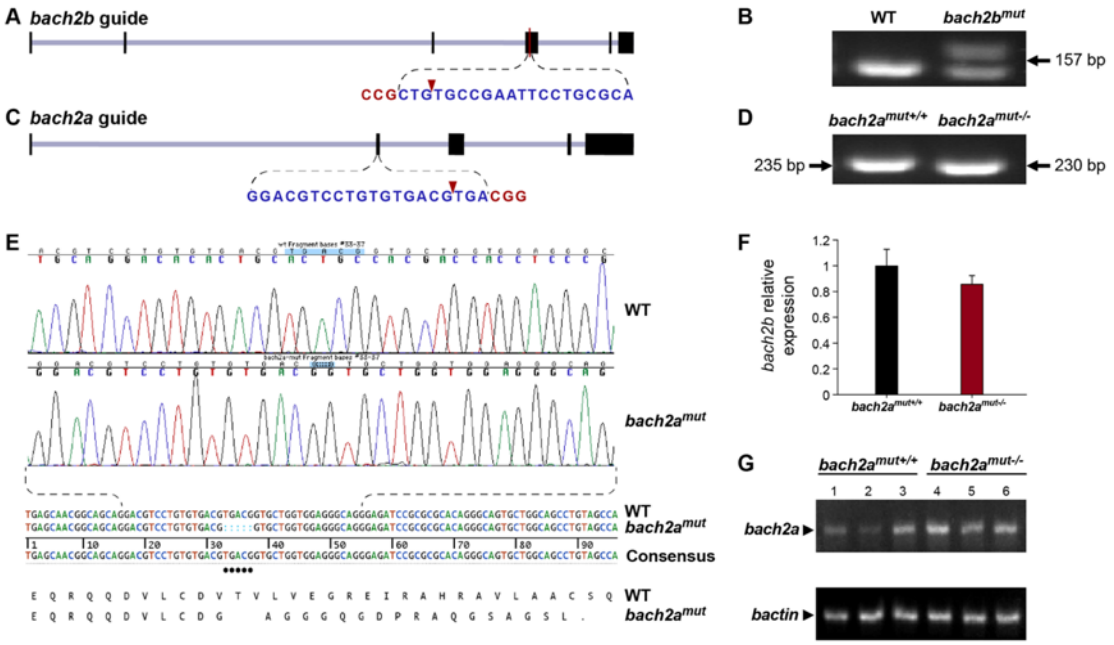

CRISPR/Cas9-mediated editing of the *bach2* paralog loci.

(A) Schematic illustration of the *bach2b* locus (XM_005160548.3) and the guide RNA targeting exon 4. The protospacer-adjacent motif (PAM) sequence is shown in red letters and the cleavage site is indicated by a red arrowhead. **(B)** Agarose gel electrophoresis of PCR products amplified from 24-hpf wild-type (WT) or *bach2b* gRNA (125 ng, *bach2b*^{mut})-injected *Tg(fli1:EGFP)*^{y1} embryos using primer sets which flank the gRNA cut sites. Arrows indicate the lengths of the resultant DNA fragments. **(C)** Schematic diagram of the *bach2a* locus (GRCz10, chr17:15666119-15734205). The CRISPR guide was designed to target exon 2, with the cleavage site (red arrowhead) located 115 bp downstream of the ATG. **(D)** Representative genotyping PCR of a wild-type (WT) and a CRIPSR/Cas9-mediated homozygous *bach2a* knockout (*bach2a*$^{mut-/-}$) *Tg(fli1:EGFP)*^{y1} embryo using primer sets which flank the gRNA cut sites. Arrows indicate the lengths of the resultant DNA fragments. **(E)** PCR-sequencing chromatograph of the *bach2a* locus in a *Tg(fli1:EGFP)*^{y1} embryo (WT) aligned with a homozygous *bach2a* knockout (*bach2a*$^{mut-/-}$). CRIPSR/Cas9-mediated genome modification at the zebrafish *bach2a* locus leads to the deletion of five base-pairs, which causes a frame shift in the protein sequence (translation shown below the DNA sequence). A stop codon (indicated by a dot in the translation) created 17 amino acids downstream of the deletion site, leading to the formation of a 57-amino-acid-long, truncated protein. **(F)** Quantitative RT-PCR validation of *bach2b* expression conducted for wild-type (*bach2a*$^{mut+/+}$) and homozygous *(bach2a*$^{mut-/-}$) 6-dpf siblings obtained from F2 *bach2a* intercross. Error bars, mean ± s.e.m.; *P=0.2466* (two independent experiments consisting of twenty single larvae in each group). **(G)** Semi-quantitative RT-PCR analysis of *bach2a* expression in wild-type (*bach2a*$^{mut+/+}$) and homozygous (*bach2a*$^{mut-/-}$) 6-dpf siblings obtained from F2 *bach2a* heterozygous intercross.

Figure 2- figure supplement 2

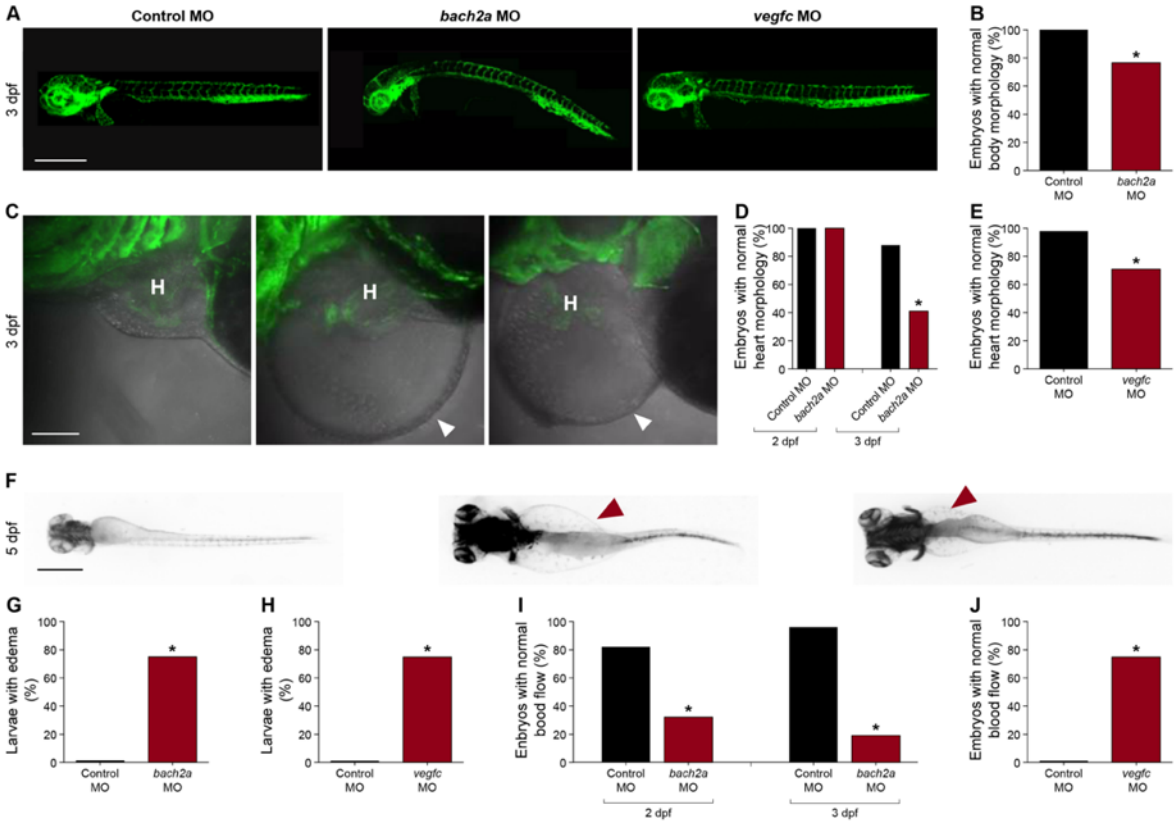

Knockdown of *bach2a* causes morphological defects in zebrafish embryos.

(A) Lateral-view confocal micrographs of full-body, 3-dpf *Tg(fli1:EGFP)*^{y1} zebrafish embryos following injection with control (10 ng, Control MO), *bach2a* (3.75 ng, *bach2a* MO) or *vegfc* (10 ng, *vegfc* MO) morpholino oligonucleotide, showing body curvature of *bach2a* morphants. Scale bar, 500 µm. **(B)** Percentage of 3-dpf *Tg(fli1:EGFP)*^{y1} zebrafish embryos with a normal morphology (no body curvature) following injection with control (10 ng, Control MO) or *bach2a* MO (3.75 ng, $n_{\text{Control MO}} = 46$; $n_{bach2a\ \text{MO}} = 47$ $^*P \leq 0.0005$). **(C)** Confocal images of the heart morphology of 3-dpf *Tg(fli1:EGFP)*^{y1} zebrafish embryos following injection with control, *bach2a* or *vegfc* MO. H marks the heart and a white arrowhead, a pericardial edema. Scale bar, 500 µm. **(D)** Quantification of 2- and 3-dpf *Tg(fli1:EGFP)*^{y1} zebrafish embryos with a normal heart morphology following injection with control MO (10 ng, Control MO) or *bach2a* MO (3.75 ng, 2 dpf: $n_{\text{Control MO}} = 16$; $n_{bach2a\ \text{MO}} = 19$; 3 dpf: $n_{\text{Control MO}} = 47$; $n_{bach2a\ \text{MO}} = 58$; $^*P < 0.0001$). **(E)** Percentage of 3-dpf *Tg(fli1:EGFP)*^{y1} zebrafish embryos with a normal heart morphology following injection with control MO (10 ng) or *vegfc* MO (10 ng, $n_{\text{Control MO}} = 54$; $n_{vegfc\ \text{MO}} = 41$; $^*P < 0.0001$). **(F)** Dorsal view of 5-dpf *Tg(fli1:EGFP)*^{y1} zebrafish larvae following injection with control MO, *bach2a* MO or *vegfc* MO. Red arrowhead indicates edema. Scale bar, 100 µm. **(G)** Percentage of 5-dpf *Tg(fli1:EGFP)*^{y1} zebrafish larvae with edema following injection with control MO (10 ng) or *bach2a* MO (3.75 ng, $n_{\text{Control MO-10ng}} = 22$; $n_{bach2a\ \text{MO}} = 28$; $^*P < 0.05$). **(H)** Quantification of 5-dpf *Tg(fli1:EGFP)*^{y1} zebrafish larvae with edema following injection with control MO (10 ng) or *vegfc* MO (10 ng, $n_{\text{Control MO}} = 22$; $n_{vegfc\ \text{MO}} = 53$; $^*P < 0.0001$). **(I)** Percentage of 2- and 3-dpf *Tg(fli1:EGFP)*^{y1} zebrafish embryos with a normal blood flow rate following injection with control MO (10 ng) or *bach2a* MO (3.75, 2 dpf: $n_{\text{Control MO}} = 14$; $n_{bach2a\ \text{MO}} = 19$; 3 dpf: $n_{\text{Control MO}} = 47$; $n_{bach2a\ \text{MO}} = 58$; $^*P < 0.05$). **(J)** Percentage of 3-dpf *Tg(fli1:EGFP)*^{y1} zebrafish embryos with a normal blood flow rate following injection with control MO (10 ng) or *vegfc* MO (10 ng: $n_{\text{Control MO}} = 54$; $n_{vegfc\ \text{MO}} = 41$; $^*P < 0.004$).

Figure 2- figure supplement 3

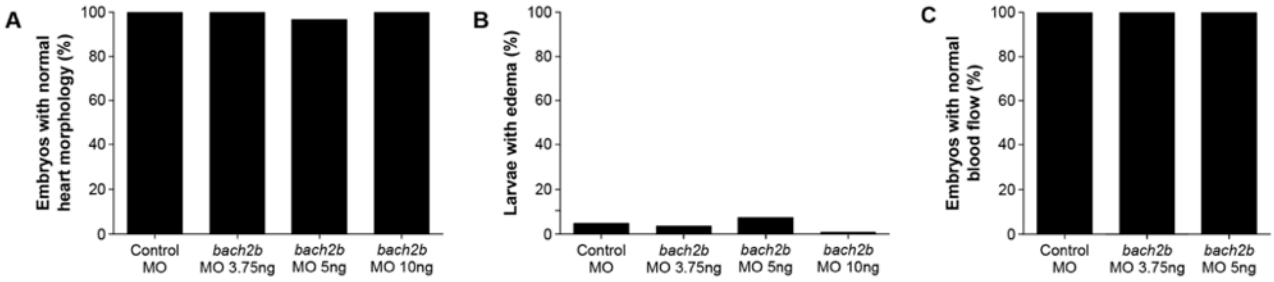

No morphological defects in *bach2b* zebrafish morphants.

(A) Percentage of 3-dpf *Tg(fli1:EGFP)*^{y1} zebrafish embryos following injection with control MO (10 ng) or *bach2b* MO (3.75, 5 or 10 ng) showing normal heart morphology ($n_{\text{Control MO}}$ = 18; $n_{bach2b\ \text{MO-3.75ng}}$ = 30; $n_{bach2b\ \text{MO-5ng}}$ = 30; $n_{bach2b\ \text{MO-10ng}}$ = 10; $P \geq 0.3878$). **(B)** Quantification of 5-dpf *Tg(fli1:EGFP)*^{y1} zebrafish larvae with edema following injection with control MO (10 ng) or *bach2b* MO (3.75, 5 or 10 ng) ($n_{\text{Control MO}}$ = 18; $n_{bach2b\text{MO-3.75ng}}$ = 30; $n_{bach2b\text{MO-5ng}}$ = 30; $n_{bach2b\text{MO-10ng}}$ = 10; P>0.9999) **(C)** Percentage of 3-dpf *Tg(fli1:EGFP)*^{y1} zebrafish embryos with a normal blood flow rate following injection with control MO (10 ng) or *bach2b* MO (3.75, 5 or 10 ng) ($n_{\text{Control MO}}$ = 18; $n_{bach2b\ \text{MO-3.75ng}}$ = 30; $n_{bach2b\ \text{MO-5ng}}$ = 30; $n_{bach2b\ \text{MO-10ng}}$ = 10; P>0.9999).

We then asked whether *bach2a* is also involved in lymphatic vessel development. To answer this question, we analyzed the effects of *bach2a* down-regulation on the formation of parachordal cells (PACs), the building blocks of the thoracic duct (TD) and the trunk lymphatic system in zebrafish (Nicenboim et al., 2015; Yaniv et al., 2006). A significantly reduced number of PAC-containing segments was detected in *bach2a* MO-injected *Tg(fli1:EGFP)*^{y1} embryos at 3 dpf (Figures 3A and 3B), recapitulating the *vegfc* MO induced phenotype (Figures 3A and 3C) and the previously reported phenotype of *vegfc* mutants (Villefranc et al., 2013). Additionally, *bach2a* morphants failed to express the lymphatic endothelial marker *lyve1*, but the expression of *vegfc* receptor *flt4* remained unchanged (Figures 3- figure supplement 1). To rule out the possibility that the observed phenotypes are a consequence of developmental delay, we assessed the formation of the TD at 4 dpf. MO-mediated downregulation of *bach2a* resulted in a significant decrease in TD formation (76%, Figures 4A and 4B) as compared to control MO-injected siblings. Similarly, 87% of *vegfc* morphants were devoid of a TD (Figures 4A and 4C), as previously reported (Shin et al., 2016; Villefranc et al., 2013). In contrast to *bach2a* morphants, *bach2b* MO (Figures 3A, 3D, 4A and 4D) and *bach2b* gRNA-injected *Tg(fli1:EGFP)*^{y1} embryos (Figures 3A, 3E, 4A and 4E) exhibited no lymphatic defects. In line with the possible genetic compensation underlying the absence of a clear angiogenic phenotype at early developmental stages (Figures 2D and 2E), injection of either a sub-dose of *bach2b*

MO or *bach2b* gRNA into the progeny of *bach2a*$^{+/-}$ intercross leads 23% of embryos to display significant lymphangiogenic defects, which were subsequently identified by genotyping as homozygous mutants (*bach2a*$^{mut-/-}$ + *bach2b* MO or *bach2a*$^{mut-/-}$ +*bach2b* gRNA) (Figures 3F, 3G and 4F and 4G). In contrast, control MO-injected *bach2a* $^{mut-/-}$ appeared normal (Figures 3F, 3G, 4F and 4G). Likewise, no lymphatic phenotype was detected in *bach2a*$^{mut-/-}$ embryos upon injection of *bach2a* MO (Figures 3F, 3G, 4F and 4G), indicating that *bach2a* MO has minimal off-target effects. Finally, cardiac and body edema, characteristic of lymphatic-related defects, were detected in *bach2a* mutants following *bach2b* MO or *bach2b* gRNA injection, but not upon *bach2a* MO administration (Figure 4- figure supplement 1). Remarkably, the phenotypic defects resulting from *bach2a* downregulation were more pronounced than those caused by the loss of *vegfc*, possibly due to the involvement of *bach2a* in additional signaling pathways (Zhou et al., 2016).

Figure 3

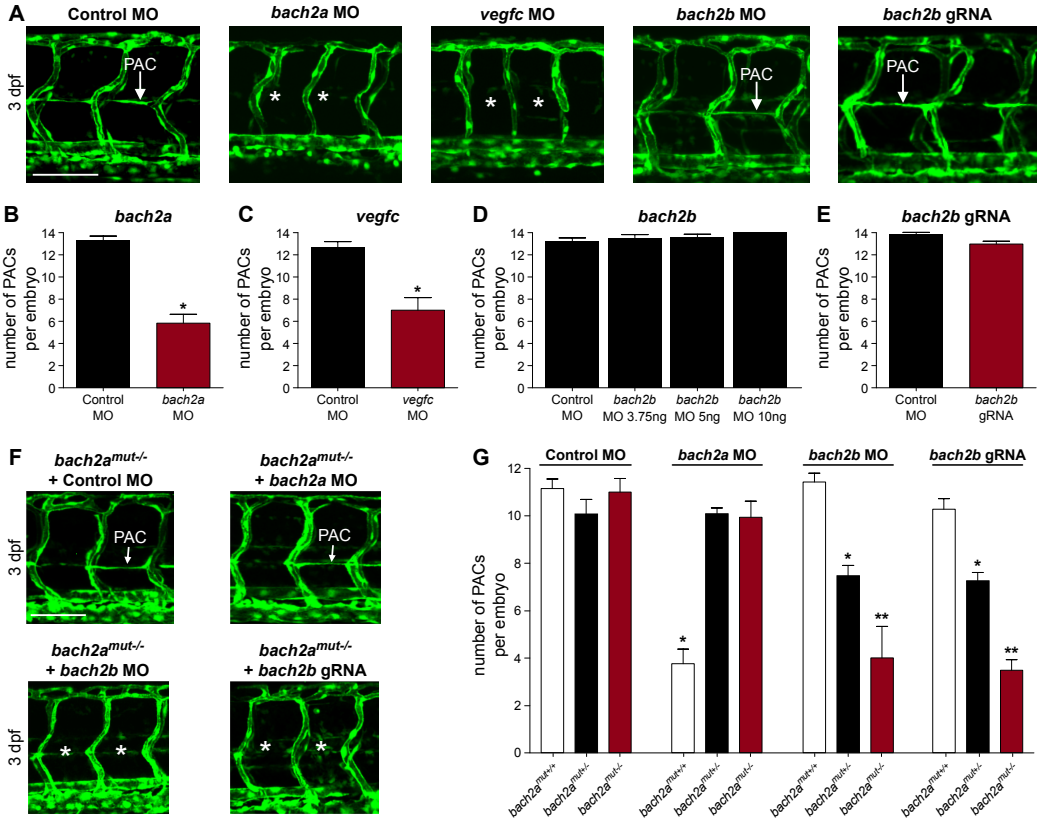

***bach2a* is essential for parachordal cell (PAC) development in zebrafish embryos.**

(A) Confocal projection of the trunk of 3-dpf *Tg(fli1:EGFP)*^{y1} embryos showing PACs (white arrow) in control MO, *bach2b* or *bach2b* gRNA-injected embryos but not following injection with *bach2a or vegfc* MO (white asterisk). Scale bar, 100 µm. **(B)** Number of PAC-containing segments (mean ± s.e.m.) in 3-dpf *Tg(fli1:EGFP)*^{y1} zebrafish embryos injected with control MO (10 ng) or *bach2a* MO (3.75 ng, $n_{\text{Control MO}} = 46$; *bach2a* MO, $n_{bach2a\ \text{MO}} = 53$; $^{*}P<0.001$). Error bars, mean ± s.e.m. **(C)** Number of PAC-containing segments

in *vegfc* MO-injected morphants (10 ng, $n_{\text{Control MO}} = 53$, $n_{vegfc\ \text{MO}} = 41$; $^{*}P<0.0001$). Error bars, mean ± s.e.m. **(D)** Number of PAC-containing segments in 3-dpf *Tg(fli1:EGFP)*^{y1} zebrafish embryos injected with indicated *bach2b* MO concentrations (3.75, 5 or 10 ng, $n_{\text{Control MO}} = 18$; $n_{bach2b\ \text{MO-3.75ng}} = 30$; $n_{bach2b\ \text{MO-5ng}} = 30$; $n_{bach2b\ \text{MO-10ng}} = 10$; $P \geq 0.2819$). Error bars, mean ± s.e.m. **(E)** Quantification of PAC-containing segments in embryos injected with *bach2b* gRNA (125 ng, $n_{\text{Control MO}} = 35$ $n_{bach2b\ \text{gRNA}} = 42$; $P=0.0615$). Error bars, mean ± s.e.m. **(F)** Confocal projection of the trunk region showing PAC-containing segments in *Tg(fli1:EGFP)*^{y1}- homozygous *bach2a* mutants (*bach2a*$^{\text{mut-/-}}$) from F2 *bach2a*$^{\text{mut+/-}}$ incross. An asterisk indicates the absence of PACs in *bach2a*$^{\text{mut-/-}}$ embryos injected with *bach2b* MO (*bach2a*$^{\text{mut-/-}}$ + *bach2b* MO) or *bach2b* gRNA (*bach2a*$^{\text{mut-/-}}$ + *bach2b* gRNA) and a white arrow, their presence. Scale bar, 100 µm. **(G)** Number of PAC-containing segments (mean ± s.e.m.) in 3-dpf embryos randomly selected from *bach2a*$^{+/-}$ F2 incross progeny injected with control MO (10 ng, $n_{bach2a\text{mut + Control MO}} = 50$; $P=0.5514$), *bach2a* MO (3.75 ng, $n_{bach2amut\ +\ bach2a\ \text{MO}} = 75$; $^{*}P<0.0001$), *bach2b* Mo (3.75 ng, $n_{bach2amut\ +\ bach2b\ \text{MO}} = 55$; $^{*}P$ and $^{**}P<0.0222$) or *bach2b* gRNA (125 ng, $n_{bach2amut\ +\ bach2b\ \text{gRNA}} = 137$; $^{*}P$ and $^{**}P<0.0001$). Following genotyping, offspring followed the expected Mendelian ratios of inheritance.

Figures 3- figure supplement 1

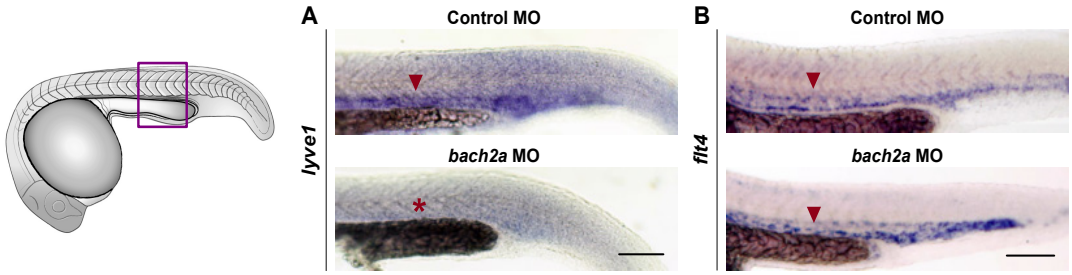

Expression of *lyve1* is impaired in *bach2a* morphants.

(A) Whole mount *in situ* hybridization comparing the expression pattern (red arrowhead) of *lyve1* in 24-hpf wild-type zebrafish embryos following injection with control or *bach2a* MO (red asterisk indicates absence of expression). **(B)** Whole mount *in situ* hybridization using *flt4* riboprobe of 24-hpf, wild-type zebrafish embryos following injection with control or *bach2a* MO. Scale bar, 100 µm.

Figure 4

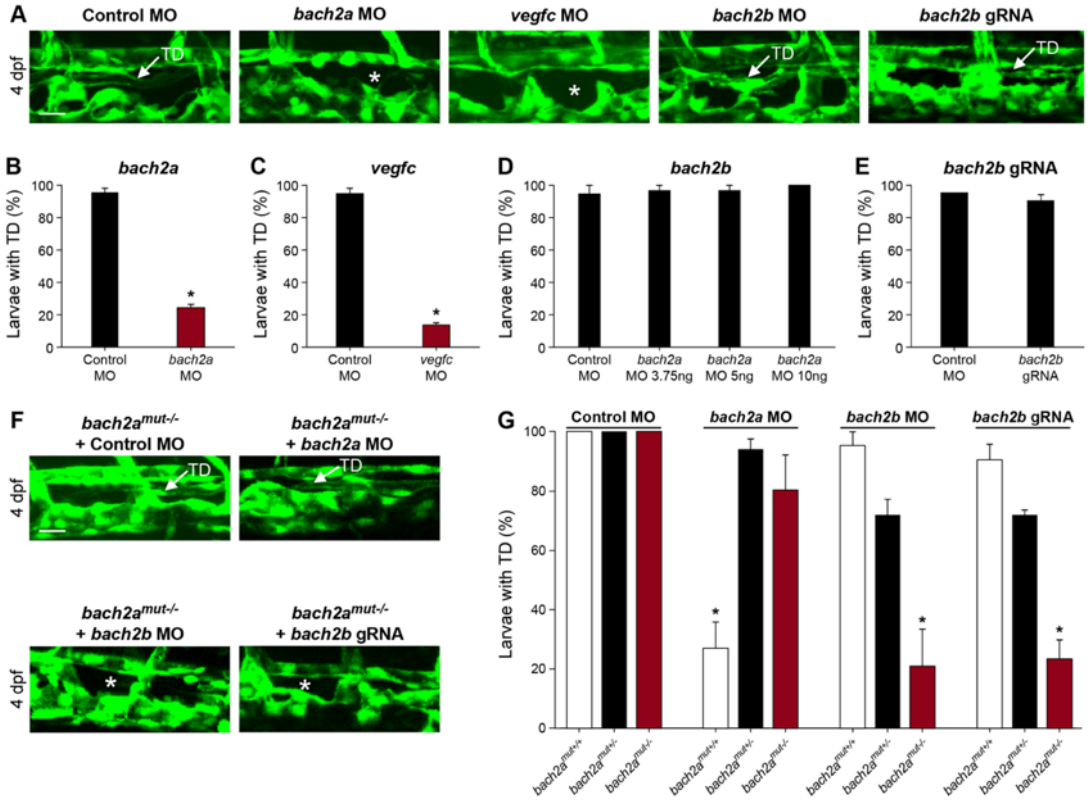

***bach2a* is necessary for thoracic duct development in zebrafish larvae.**

(A) Confocal images of the thoracic duct (TD) in 4-dpf control MO- (10 ng), *bach2a* MO-(3.75 ng), *vegfc* MO- (10 ng), *bach2b* MO- (10 ng) or *bach2a* gRNA-injected *Tg(fli1:EGFP)*^{y1} larvae. A white arrow indicates the presence of a TD and a white asterisk, its absence. Scale bar, 20 µm. **(B)** Percentage of 4-dpf *Tg(fli1:EGFP)*^{y1} larvae with an intact thoracic duct (TD) following injection with control MO (10 ng) or *bach2a* MO (3.75 ng, $n_{\text{Control MO}} = 46$; $n_{bach2a\ \text{MO}} = 52$). Error bars, mean ± s.e.m.; **P*<0.0001. **(C)** Percentage of larvae with a TD following injection with *vegfc* MO (10 ng, $n_{\text{Control MO}} = 46$; $n_{vegfc\text{MO}} = 52$). Error bars, mean ± s.e.m.; **P*<0.0001. **(D)** Quantification of *bach2b* morphants with an intact TD following injection with indicated *bach2b* MO concentrations (3.75, 5 or 10 ng, $n_{\text{Control MO}} = 18$; $n_{bach2b\ \text{MO-3.75ng}} = 30$; $n_{bach2b\ \text{MO-5ng}} = 30$; $n_{bach2b\ \text{MO-10ng}} = 10$; $P \geq 0.1356$). Error bars, mean ± s.e.m. **(E)** Percentage of TD-containing larvae injected with *bach2b* gRNA (125 ng, $n_{\text{Control MO}} = 35$ $n_{bach2b\ \text{gRNA}} = 42$; $P = 0.5461$). Error bars, mean ± s.e.m. **(F)** Confocal images of a TD (white arrow) in 4-dpf *Tg(fli1:EGFP)*^{y1} - homozygous *bach2a* mutants (*bach2a*$^{\text{mut-/-}}$) derived from bach2a$^{\text{mut+/-}}$ F2 incross. An asterisk indicates absence of a TD and a white arrow, its presence. Scale bar, 20 µm. **(G)** Analysis of *Tg(fli1:EGFP)*^{y1} 4-dpf progeny obtained from F2 *bach2a* heterozygous intercross. Random selection from the pool of siblings injected at the one-cell stage with control MO (10 ng, $n_{bach\text{mut + Control MO}} = 50$), *bach2a* MO (3.75 ng, $n_{bach2amut + bach2a\ \text{MO}} = 75$), *bach2b* MO (3.75 ng, $n_{bach2amut + bach2b\ \text{MO}} = 55$) or *bach2b* gRNA (125 ng, $n_{bach2amut + bach2b\ \text{gRNA}} = 137$) were found to maintain, following genotyping, the expected Mendelian ratios of inheritance. Error bars, mean ± s.e.m.; **P*<0.0003.

Figure 4- figure supplement 1

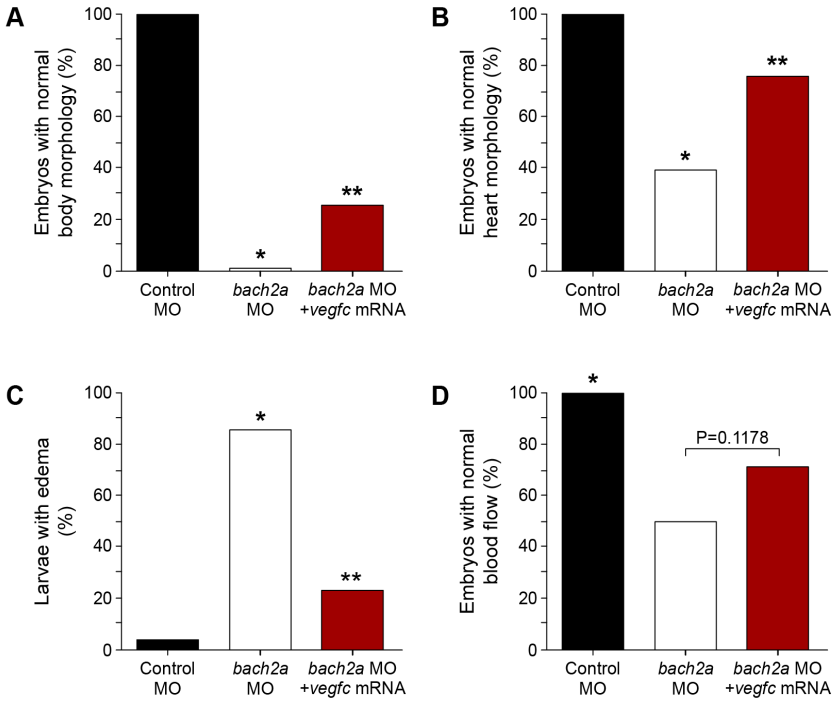

Morphological abnormalities in homozygous *bach2a* mutants following *bach2b* knockdown.

(A) Fluorescent images of homozygous *bach2a* (*bach2a*$^{mut-/-}$) siblings obtained from F2 *bach2a* heterozygous intercross injected at the one-cell stage with control (10ng, Control MO) or *bach2b* MO (3.75 ng). Scale bar, 500 µm. **(B)** Bright-field images corresponding to the larvae presented in panel A. Red arrowhead indicates cardiac edema. Scale bar, 500 µm. **(C)** Lateral view of 6-dpf homozygous *bach2a* (*bach2a*$^{mut-/-}$) siblings obtained from F2 *bach2a* heterozygous intercross injected with control (10 ng, Control MO), *bach2a* (3.75 ng, *bach2a* MO), *bach2b* (3.75 ng, *bach2b* MO) morpholino or *bach2b* guide RNA (125 ng, *bach2b* gRNA). Red arrowhead indicates cardiac edema, while body edema is indicated by a black arrow. Scale bar, 500 µm.

Taken together, these findings demonstrate that knockdown of *bach2a* through MO injection results in the formation of defective blood and lymphatic vascular plexuses, despite the presence of the *bach2b* paralog, indicating that *bach2a* is a major contributor to this phenotype. However, knockout of *bach2a* expression (in mutants) triggers a functional compensation by *bach2b,* suggesting that the two *bach2* genes may share partially overlapping functions, which allows them to compensate for each other's loss during blood and lymph vessel development. Accordingly, it was suggested that BACH1 and BACH2 act in a complementary manner to maintain normal alveolar macrophage function and surfactant homeostasis in the lung (Ebina-Shibuya et al., 2016). Similar phenotypic differences between mutants and transient knockdown animals were observed in various model systems, some of which were attributed to genetic compensation (El-Brolosy et al., 2019; El-Brolosy & Stainier, 2017; Rossi et al., 2015).

BACH1 promotes angiogenesis and lymphangiogenesis during tumor expansion in mouse models

In light of the perception that cancers frequently reactivate embryonic developmental signaling cascades to promote their expansion and aggressiveness, resulting in metastasis and poor patient outcome, we decided to evaluate the contribution of BACH to vascular remodeling during tumor progression. Emerging evidence point to BACH1, a ubiquitously expressed protein, as a tumor-promoting factor that acts via multiple intracellular signaling cascades (Alvarez & Woolf, 2011; Yun et al., 2011). Recently, higher levels of BACH1 were found to be associated with poor prognosis in human ovarian cancer (Han et al., 2019) and to promote lung cancer metastasis (Lignitto et al., 2019; Wiel et al., 2019). BACH1 has been established as a major regulator of breast cancer bone metastasis (Liang et al., 2012) and was postulated as a potential novel therapeutic candidate for cancer treatment (Davudian, Mansoori, Shajari, Mohammadi, & Baradaran, 2016; J. Lee et al., 2019). To assess whether enhanced expression of BACH1 in tumor cells can stimulate blood and lymphatic vessel expansion during tumor progression as well as metastatic spread, we analyzed various ovarian and lung mouse tumors (Figures 5 and
Figure 5- figure supplement 1). Inoculation of human ovarian clear cell carcinoma ES2 cells into the peritoneal cavity of immune-deficient CD-1 nude female mice has been established as a model of metastatic ovarian cancer (Shaw, Senterman, Dawson, Crane, & Vanderhyden, 2004). In this study, we used this model to evaluate the effects of ectopic expression of *BACH1* in human ovarian ES2 carcinoma cells (Figure 5). Twenty days post-injection, metastases were detected in the diaphragm of animals injected with *BACH1*-overexpressing ES2 cells. An increase in $CD34^+$ tumor-associated blood vessel density was apparent in diaphragm specimens derived from mice injected with *BACH1*-overexpressing cells, as compared to control ES2 cells (Figures 5A and 5B). Similar differences in the intratumoral blood vasculature were observed following subcutaneous inoculation of either *BACH1*-overexpressing ES2 cells (Figure 5- figure supplement 1A, 1B and 1C) or *Bach1*-overexpressing mouse D122 Lewis Lung Carcinoma cells (Eisenbach et al., 1984) (Figure 5-figure supplement 1E, 1F and 1G). These results indicate that, in addition to its role in embryonic vascular development, BACH1 promotes tumor angiogenesis.

Numerous reports suggest that, in addition to blood vessel formation, lymphangiogenesis and lymphatic vessel remodeling are pivotal events for tumor expansion and metastatic spread (Stacker et al., 2014). We thus examined the effects of BACH1 on the lymphatic vasculature

in various mouse tumor models. To gain insight into the 3D complexity of the lymphatic network within intact tumors, we subjected ES2 subcutaneous xenografts to a modified CLARITY (Clear, Lipid-exchanged, Anatomically Rigid, Imaging-compatible, Tissue hYdrogel) technique (K. Chung et al., 2013; Hama et al., 2011; Oren et al., 2018), along with LYVE1 immunofluorescence staining. A robust increase in lymphatic vessel density was observed in *BACH1*-overexpressing tumors as compared to control-derived ES2 tumors (Figure 5C, Figure 5- Movie 1 and Figure 5- Movie 2). Morphometric analyses indicate a significant increase in the relative area fraction occupied by LYVE1^{+} tumor-associated lymphatic vessels in diaphragm specimens removed from mice injected with *BACH1*-overexpressing ES2 cells (Figures 5D and 5E). In addition, enlarged lymph vessels were observed in the peritumoral region of subcutaneous tumors derived from BACH1-overexpressing ES2 and D122 cells (Figure 5- figure supplement 1D and 1H, respectively). Expansion of the lymph vessels in the diaphragms of *BACH1*-overexpressing tumors was associated with increased cell infiltration (arrow, Figure 5D). Co-immunofluorescence using antibodies directed against LYVE1 and Cytokeratin 7, an antigen expressed in ES2 cells (Stimpfl et al., 1999), revealed that the metastasizing cells originated from the transplanted ES2 tumor cells (arrow, Figure 5F). This potential of *BACH1* to promote tumor cell invasion was further confirmed by an *in vitro* invasion assay demonstrating a ~two-fold increase in the invasion abilities of *BACH1*-overexpressing as compared to control ES2 cells (Figures 5G and 5H). These data indicate that in mouse models BACH1 remodels vascular architecture and promotes metastatic spread of tumor cells via the lymphatic vessels.

Figure 5

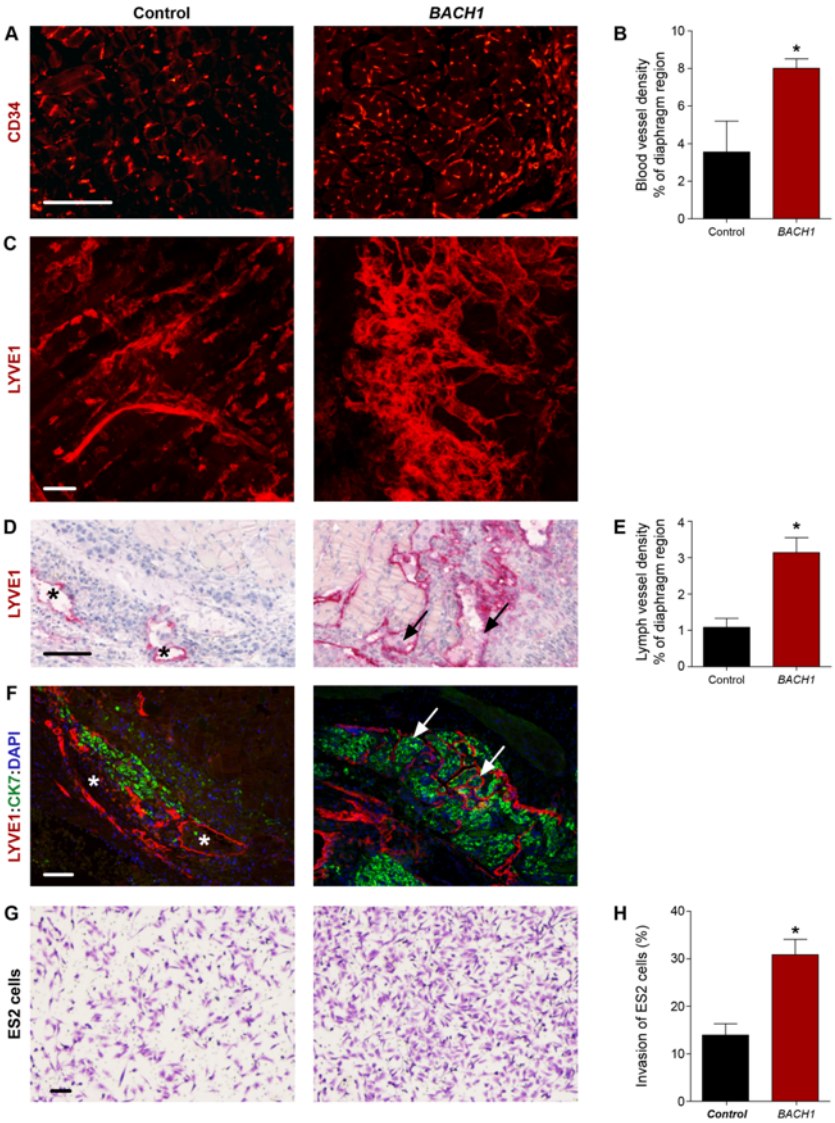

***BACH1* promotes angiogenesis and lymphangiogenesis during ovarian tumor progression in mouse models.**

Ex vivo analysis of subcutaneous xenografts and diaphragm specimens excised from CD-1 nude female mice implanted with control (Control) or *BACH1* ectopically expressing (*BACH1*) human ovarian clear cell carcinoma ES2 cells. **(A)** Immunofluorescence labeling of blood vessels using anti-CD34 antibodies in diaphragm specimens excised from mice injected intraperitoneally with control or *BACH1*-expressing human ES2 cells. Scale bar, 100 µm. **(B)** Morphometric analysis of the diaphragm relative region covered by $CD34^+$ blood vessels. Diaphragms were excised from mice inoculated intraperitoneally with either control (Control, n=3) or *BACH1*-overexpressing (*BACH1*, n=7) ES2 cells (mean ± s.e.m.; $*P= 0.0304$). **(C)** Confocal z-projection images of control and *BACH1*-overexpressing subcutaneous-ES2 ovarian carcinoma xenografts subjected to LYVE1 immunofluorescence staining along with a modified CLARITY technique. Images demonstrate the complexity of the lymphatic vasculature. Scale bar, 100 µm. 3D reconstructions of the stacks are available in Supplementary movies 1 and 2. **(D)** Lymphatic vessel immunostaining, using anti-LYVE1 antibodies, of diaphragm specimens excised from mice injected intraperitoneally with control or *BACH1*-overexpressing ES2 ovarian carcinoma cells. A black arrow indicates infiltration of cells into the lymphatic

vessel and an asterisk, their absence. Scale bar, 100 µm. **(E)** Morphometric analysis of the diaphragm relative region covered by LYVE1$^+$ lymph vessels. Diaphragms were excised from mice inoculated intraperitoneally with either control (Control, n=6) or *BACH1*-overexpressing (*BACH1*, n=9) ES2 cells (mean ± s.e.m.; *P=0.0047). **(F)** Immunofluorescence double staining of LYVE1$^+$ lymphatic vessels (red) and cytokeratin 7 (CK7, green) of a diaphragm excised from mouse inoculated intraperitoneally with either control or *BACH1*-overexpressing ES2 cells. Nuclei were counterstained with DAPI (blue). A white arrow indicates infiltration of tumor cells into the lymphatic vessels and an asterisk, their absence. Scale bar, 100 µm. **(G)** Transwell Matrigel invasion assay performed *in vitro* with ES2 ectopically expressing *BACH1* and control cells. The crystal violet dye staining images of the lower chambers are shown. Scale bar, 100 µm. **(H)** Percentage of ES2 cells that invaded through the Matrigel matrix (as in panel g) normalized to total cell number (n = 2 for each group, in duplicates; mean ± s.e.m.; *P=0.0209).

Figure 5- figure supplement 1

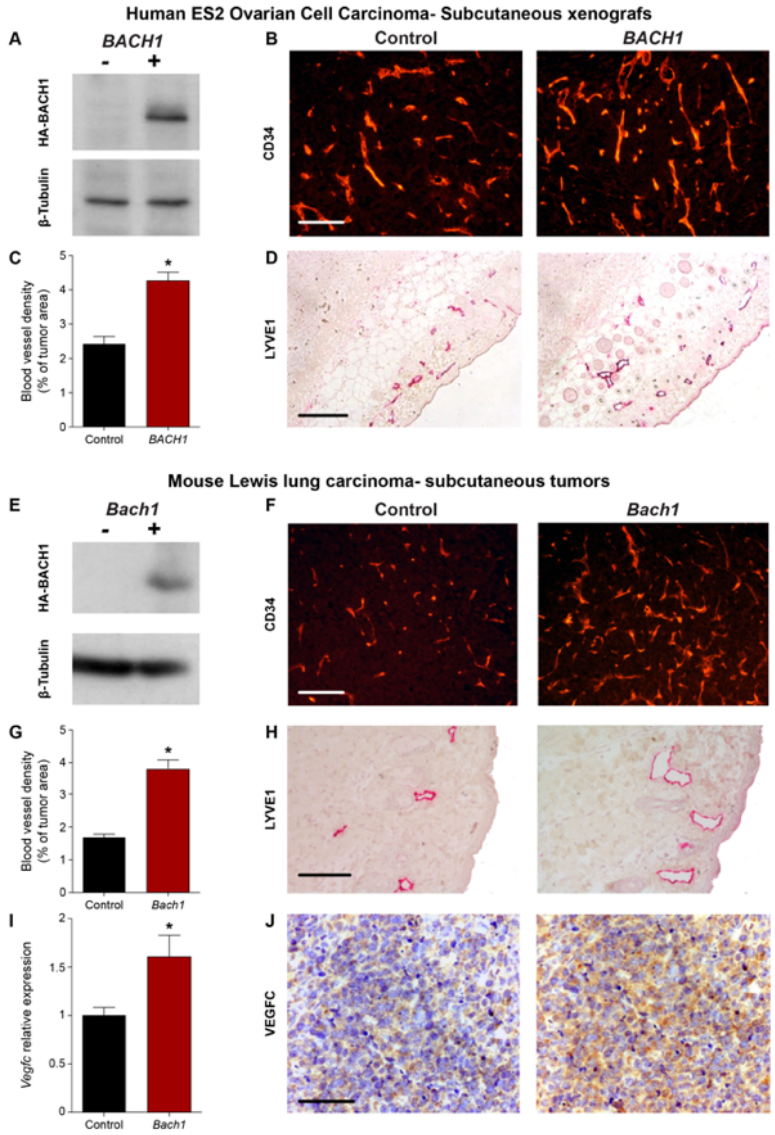

BACH1 overexpression in mouse tumor models stimulates angiogenesis, lymphangiogenesis and induction of VEGFC expression.

Analysis of subcutaneous tumor specimens (two mouse models: human ovarian clear cell carcinoma ES2 cells in CD-1 nude mice and mouse D122 Lewis lung carcinoma cells in C57BL/6 black mice) excised from mice implanted with either ectopic overexpression of HA-BACH1 or control cells expressing an empty vector

(Control). **(A)** Western blot detecting HA-BACH1 and β-Tubulin in protein extracts from control (-) or *BACH1* (+)-ectopically-expressing ES2 cell. **(B)** Immunofluorescence labeling of blood vessels using anti-CD34 antibodies of subcutaneous tumors excised from mice inoculated with control (Control) or *BACH1* (*BACH1*)-ectopically-expressing human ES2 cells. **(C)** Morphometric analysis of the relative coverage of $CD34^+$ blood vessels within the tumor area (n = 5 in each group; mean ± s.e.m.; *P<0.0001). **(D)** Immunohistochemical staining of lymphatic endothelial cells using anti–LYVE1 antibodies. Scale bar, 100 µm. **(E)** Western blot detecting HA-BACH1 and β-Tubulin in protein extracts from control (-) or *Bach1* (+)-ectopically-expressing mouse D122 Lewis lung carcinoma cells. **(F)** Immunofluorescence labeling of blood vessels using anti-CD34 antibodies of subcutaneous tumor specimens excised from mice inoculated with control (Control) or *Bach1* (*Bach1*)-ectopically-expressing mouse D122 Lewis lung carcinoma cells. **(G)** Morphometric comparison between the coverage of $CD34^+$ blood vessels within the tumor area of control (Control, n = 9) or *Bach1*-overexpressing (*Bach1*, n = 8) D122 Lewis lung cells (mean ± s.e.m.; *P<0.0001). **(H)** Immunohistochemical staining of lymphatic endothelial cells using anti-LYVE1 antibodies. **(I)** Quantitative RT-PCR validation of *Vegfc* mRNA levels in *Bach1*-overexpressing mouse D122 Lewis lung tumors compared to control tumor (n = 6 per group; mean ± s.e.m.; *P<0.05). **(J)** Immunohistochemical labeling of tumor sections using anti-VEGFC antibodies and counterstaining with hematoxylin (blue). Scale bar, 100 µm.

Figure 5- Movie 1

Lymphatic vessel complexity in a control tumor.

A movie demonstrating the lymphatic vessel density in a control subcutaneous ES2 ovarian carcinoma xenograft subjected to LYVE1 immunofluorescence staining along with a modified CLARITY technique. Scale bar, 100 µm.

Figure 5- Movie 2

Lymphatic vessel complexity in *a BACH1*-overexpressing tumor.

A movie demonstrating the lymphatic vessel density in a subcutaneous-*BACH1*-overexpressing ES2 ovarian carcinoma xenograft subjected to LYVE1 immunofluorescence staining along with a modified CLARITY technique. Scale bar, 100 µm.

BACH and VEGFC are functionally linked

Next, we investigated the molecular mechanisms underlying BACH activity. Since BACH proteins can directly bind to the promoter of their target genes (Ogawa et al., 2001; Warnatz et al., 2011; Yun et al., 2011), we assessed the ability of the binding sites in the *VEGFC* promoter region identified *in silico* (Figures 1A and Figure 6A) to interact with BACH. Chromatin immunoprecipitation (ChIP) was performed on human ovarian clear cell carcinoma ES2 cells, overexpressing *BACH1* tagged with a human influenza hemagglutinin (HA) tag (Figure 5- figure supplement 1A). We observed that specific sequences from both proximal and distal regulatory regions were enriched in the presence of antibodies against either HA or BACH1, indicating that both sites are transcriptionally functional (Figure 6B). To investigate the functional significance of two potential BACH binding sites, promoter-reporter constructs were engineered with deletion of the BACH binding sites, either

separately or concurrently. Disruption of the proximal site led to a 23% increase in *VEGFC* basal promoter activity (Figures 6C and 6D), supporting an inhibitory role. In contrast, deletion of the distal binding site individually or in combination with the proximal site resulted in an 86% reduction in *VEGFC* basal promoter activity (Figures 6C and 6D), suggesting a pivotal role in basal promoter functioning. Additionally, overexpression of *BACH1* in human ovarian ES2 carcinoma cells induces a significant increase in VEGFC expression (Figure 6E), strongly supporting a genetic and functional link between these two factors.

Figure 6

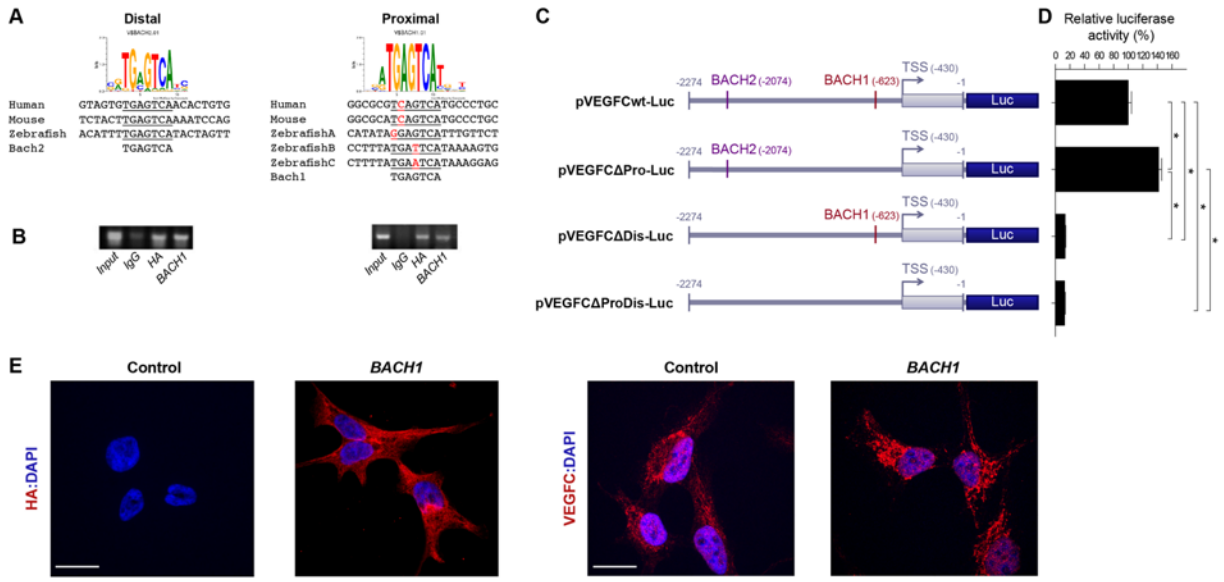

BACH1 and *VEGFC* genetically interact.

(A) Conservation of BACH sites in human, mouse and zebrafish. The distal site is completely conserved. The proximal site is fully conserved between mouse and human, while there are three BACH sites at very close proximity in zebrafish. All proximal sites differ by one nucleotide from the consensus sequence. **(B)** Chromatin immunoprecipitation (ChIP) assay, followed by PCR measurements, was performed using primer mapping to the above human BACH proximal and distal regulatory sites and DNA precipitated with non-specific IgG, HA-tag or BACH1 antibodies. **(C)** Schematic representation of the wild-type human VEGFC promoter-driven luciferase (Luc) reporters (blue) (pVEGFCwt-Luc) and of three constructs deleted either from proximal (nt. -623 to -603, pVEGFCΔPro-Luc) or distal (nt. -2074 to -2054, pVEGFCΔDis-Luc) BACH binding sites or a combination thereof (nt -623 to -603 and -2074 to -2054, pVEGFCΔProDis-Luc). Numbers refer to the nucleotide positions relative to ATG (translation initiation). TSS, transcription start site. **(D)** Quantification of dual-luciferase activity in human ES2 cells driven from pVEGFCwt-Luc, pVEGFCΔPro-Luc, pVEGFCΔDis-Luc and pVEGFCΔProDis-Luc constructs. Relative luciferase activity is shown as a percentage of the pVEGFCwt-Luc value (mean ± s.e.m., $n = 3$). *$P<0.0001$ (E) Immunofluorescence staining of human ES2 cells stably expressing either an empty pIRES vector (Control) or N-terminally HA-tagged *BACH*1 (BACH1) with antibodies directed against the HA tag (red, left panel) or against VEGFC (red, right panel). Nuclei were counterstained with DAPI (blue). Scale bar, 20 µm.

To investigate whether these results are recapitulated *in vivo*, we analyzed the effect of *bach2a* knockdown on *vegfc* expression during zebrafish development. A marked downregulation of *vegfc* expression was observed in *bach2a* morphants (Figure 7A). This effect was specific for *bach2a*, as *vegfc* expression remained intact in *bach2b* MO-injected embryos (Figure 7- figure supplement 1). We then attempted to rescue the phenotypes of *bach2a* morphants by overexpressing *vegfc* mRNA. Co-injection of *in vitro* transcribed *vegfc* mRNA and *bach2a* MO partially restored PHBC formation at 30 hpf (Figures 7B and 7C). Similarly, the number of PAC-containing segments increased by approximately 50% following co-injection of *bach2a* MO and *vegfc* mRNA (Figures 7D and 7E) and a two-fold recovery in TD formation was detected (Figures 7F and 7G). In addition, pericardial and body edema, as well as reduced blood flow, were partially restored following an injection of *vegfc* mRNA (Figure 7- figure supplement 2).

Finally, we addressed the molecular basis of the BACH1 and VEGFC interaction during tumor progression in the various mouse tumor models. VEGFC expression was specifically elevated in BACH1-overexpressing ES2 and D122 tumors both at the protein (Figures 7H, and Figure 5- figure supplement 1J, respectively) and mRNA level (Figures 7I and Figure 5- figure supplement 1I), with no significant changes in the mRNA levels of either VEGFA or VEGFB (Figure 7- figure supplement 3). Similarly, the mRNA expression levels of *MMP1,* a recognized transcription target of BACH1 (Liang et al., 2012; Yun et al., 2011), were significantly elevated in subcutaneous *BACH1*-overexpressing ES2 xenografts (Figure 7I). Collectively, these results highlight BACH as a novel regulator of blood and lymphatic vessel formation during both embryonic development and mouse tumor expansion, placing it upstream of VEGFC in these cascades.

Figure 7

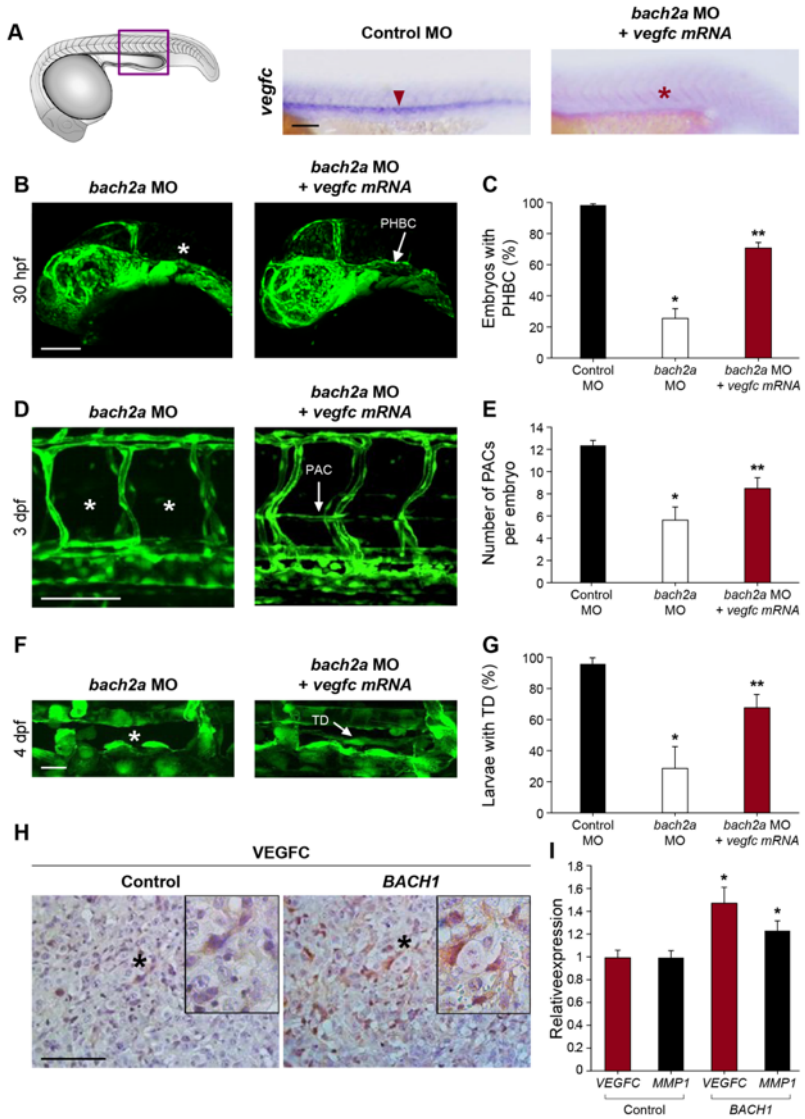

BACH mediates angiogenesis and lymphangiogenesis in a VEGFC-dependent manner.

(A) Whole-mount *in situ* hybridization of 24-hpf, wild-type zebrafish embryos demonstrating the expression of *vegfc* mRNA following injection with control MO (Control MO 10 ng, red arrowhead) and the absence of its expression in embryos injected with specific MO targeting *bach2a* (3.75 ng, *bach2a* MO, red asterisk). Scale bar, 100 µm. **(B)** Confocal images of 30-hpf *Tg(fli1:EGFP)*^{y1} embryos co-injected with specific MOs targeting *bach2a* (3.75 ng) and *in vitro* transcribed *vegfc* mRNA (800 pg, *bach2a* MO + *vegfc* mRNA) demonstrating the restoration of PHBC (white arrow). **(C)** Percentage of rescued PHBC defects in 30-hpf *Tg(fli1:EGFP)*^{y1} embryos following co-injection with *bach2a* MO (3.75 ng) and *vegfc* mRNA (800 pg), $n_{\text{Control MO}} = 56$; $n_{bach2a\ \text{MO}} = 58$; $n_{bach2a\ \text{MO} + vegfc\ \text{mRNA}} = 56$). Error bars, mean ± s.e.m.; * or ***P*<0.0001. **(D)** Rescue of PAC development in 3-dpf *Tg(fli1:EGFP)*^{y1} embryos following the co-injection of *bach2a* MO and *vegfc* mRNA (*bach2a* MO + *vegfc* mRNA; PACs are indicated by a white arrow). Scale bar, 100 µm. **(E)** Quantification of the number of PAC-containing segments (mean ± s.e.m.) in 3-dpf *Tg(fli1:EGFP)*^{y1} embryos following the co-injection of *bach2a* MO (3.75 ng) and *vegfc* mRNA ($n_{\text{Control MO}} = 47$; $n_{bach2a\ \text{MO}} = 27$; $n_{bach2a\ \text{MO} + vegfc\ \text{mRNA}} = 54$; * or ***P*<0.01). **(F)** TD formation in 4-dpf *Tg(fli1:EGFP)*^{y1} embryos co-injected with *bach2a* MO and *vegfc* mRNA (*bach2a* MO + *vegfc* mRNA; TD is indicated by a white arrow). Scale bar, 20 µm. **(G)** Percentage of 4-dpf *Tg(fli1:EGFP)*^{y1} embryos showing normal TD following *bach2a* MO and *vegfc* mRNA injection (*bach2a* MO + *vegfc* mRNA). ($n_{\text{Control MO-10ng}} = 32$; $n_{bach2a\text{MO}} = 65$; $n_{bach2a\text{MO} + vegfc\ \text{mRNA}} = 68$) Error bars, mean ± s.e.m.; * or ***P*<0.01 **(H)** Immunohistochemistry labeling of control (Control) or *BACH1* (*BACH1*) ectopically expressing ES2 ovarian carcinoma xenograft specimens using anti-VEGFC antibodies

and counterstaining with hematoxylin (blue). Black asterisk localizes the region magnified in the black frame. Scale bar, 100 µm. **(I)** Quantitative RT-PCR measurement of *VEGFC* and *MMP1* mRNA expression in xenograft initiated either from control or *BACH1*-overexpressing ES2 cells (n=5 in each group; mean ± s.e.m.; *P<0.05).

Figure 7- figure supplement 1

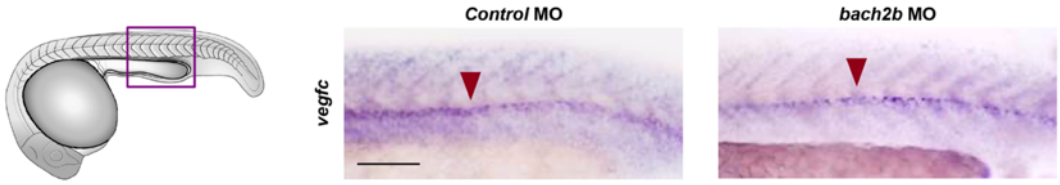

***Vegfc* mRNA levels are not affected in *bach2b* morphants.**

Whole mount in *situ* hybridization presenting the expressions of *vegfc* in 24-hpf embryos injected with control or *bach2b* MO. Presence of expression is indicated by a red arrowhead. Scale bar, 100 µm.

Figure 7- figure supplement 2

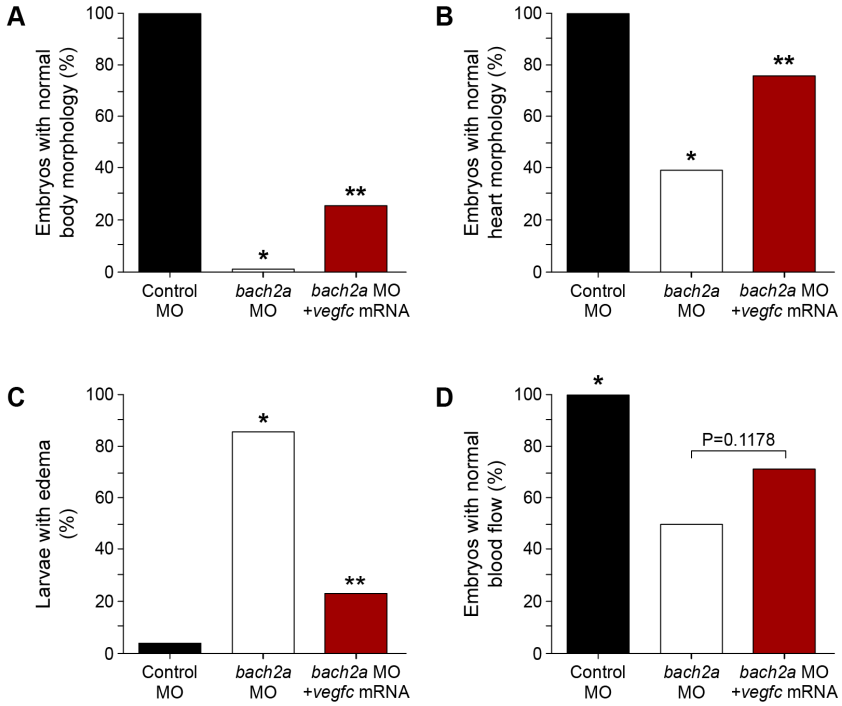

***Vegfc* mRNA partially rescues morphological defects in *bach2a* morphants.**

(A) Quantification of 3-dpf *Tg(fli1:EGFP)*^{y1} zebrafish embryos injected with control (10 ng), *bach2a* (3.75 ng) MO or co-injection with *bach2a* MO (3.75 ng) together with *in vitro* transcribed *vegfc* mRNA (800 pg) showing normal body morphology ($n_{\text{Control MO}}$ = 25; $n_{bach2a\ \text{MO}}$ = 41; $n_{bach2a\ \text{MO} + vegfc\ \text{mRNA}}$ = 43; * or **P<0.05). **(B)** Percentage of normal heart morphology (3.5 dpf, b: $n_{\text{Control MO}}$ = 54; $n_{bach2a\ \text{MO}}$ = 28; $n_{bach2a\ \text{MO} + vegfc\ \text{mRNA}}$ = 33; * or **P<0.05). **(C)** Percentage of rescued body edema in 5-dpf larvae ($n_{\text{Control MO}}$ = 25; $n_{bach2a\ \text{MO}}$ = 66; $n_{bach2a\ \text{MO} + vegfc\ \text{mRNA}}$ = 70; *P ≤0.0001). **(D)** Quantification of normal blood flow rate of 3-dpf embryos ($n_{\text{Control MO}}$ = 54; $n_{bach2a\ \text{MO}}$ = 35; $n_{bach2a\ \text{MO} + vegfc\ \text{mRNA}}$ = 28). *P<0.05.

Figure 7- figure supplement 3

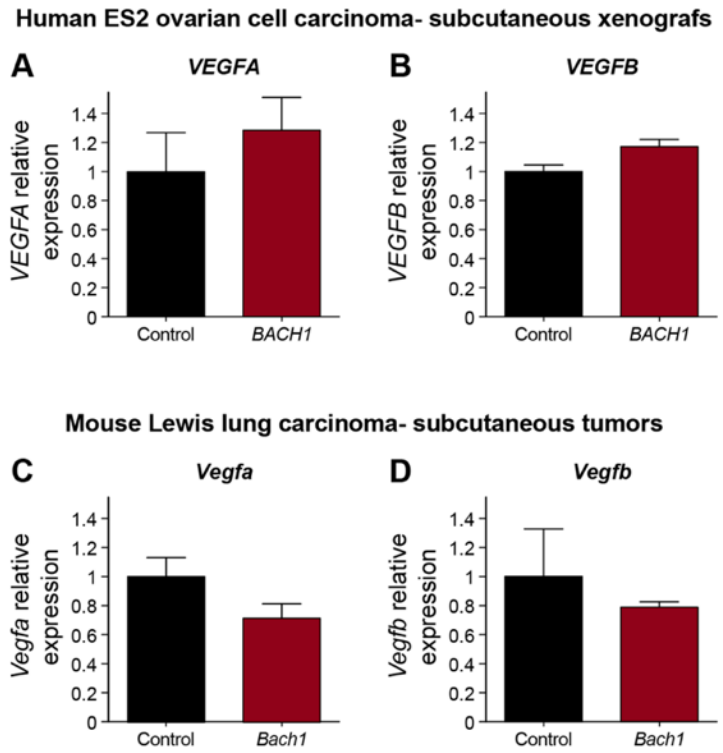

The expression of VEGFA and VEGFB during tumor growth in mouse models is not BACH1 dependent.

(**A**) Quantitative RT-PCR measurement of *VEGFA* expression conducted on xenograft initiated either from control or *BACH1*-overexpressing ES2 cell (n=5 in each group; mean ± s.e.m.; $P = 0.6857$). (**B**) Quantitative RT-PCR validation of *VEGFB* expression conducted either on control or *BACH1*-overexpressing ES2 xenografts (n = 5 in each group; mean ± s.e.m.; P=0.0556). (**C**) Quantitative RT-PCR measurement of *Vegfa* mRNA levels in *Bach1*-overexpressing mouse D122 Lewis lung tumors compared to control tumor (n = 6 per group; mean ± s.e.m.; P=0.2500). (**D**) Quantitative RT-PCR validation of *Vegfb* mRNA levels in *Bach1*-overexpressing mouse D122 Lewis lung tumors compared to control tumor (n = 6 per group; mean ± s.e.m.; P>0.9999).

The expression of *BACH1* and *VEGFC* correlates during human cancer progression

Metastatic spread of cancer cells from primary solid tumors to sentinel lymph nodes and distant tissues and organs is one of the hallmarks of malignant neoplasms (Valastyan & Weinberg, 2011), responsible for the majority of human cancer-related deaths. Neoplastic cell dissemination may occur either via blood vessels or via the lymphatic system (Paduch, 2016). VEGFC is one of the key factors promoting malignant cell spread, as demonstrated both in mouse tumor models (Ma et al., 2018; Mandriota et al., 2001; Skobe et al., 2001) and during human cancer progression (J. C. Chen et al., 2012; H. Jiang, Shao, & Zhao, 2014; Rinderknecht & Detmar, 2008; Thiele & Sleeman, 2006). Similarly, it was shown that BACH1 promotes the metastasis of breast cancer through different molecular mechanisms (J. Lee et al., 2014; U. Lee et al., 2013; Liang et al., 2012) and its stabilization in lung

adenocarcinoma is associated with increased metastatic dissemination and poor survival (Lignitto et al., 2019; Wiel et al., 2019). To substantiate the pathophysiological relevance of the interaction between *BACH1* and *VEGFC*, we carried out an *in silico* analysis of publicly available gene-expression data generated by The Cancer Genome Atlas (TCGA) Research Network (https://cancergenome .nih.gov/). We analyzed RNA-sequencing-derived data regarding aberrant gene expression in specimens taken from melanoma and lung adenocarcinoma (LUAD) human cancer patients. Melanoma is one of the commonest forms of skin cancer, while LUAD is at present the most common lung cancer subtype among non-smokers. In both cancers, while the early-stage is curable by surgical resection, lymphatic metastasis results in poor prognosis. Interestingly, we found that *BACH1* expression positively and significantly correlates with the expression of *VEGFC* in human melanoma and LUAD cancer progression (Figure 8). Specifically, *BACH1* and *VEGFC* expression are significantly higher in samples from melanoma patients clinically diagnosed with lymph node metastatic spread, as compared to those with primary tumors (Figure 8A). Similarly, the expression of *BACH1* and *VEGFC* were significantly augmented in specimens derived from clinical stage III LUAD patients in comparison to stage I and II (Figure 8B). According to the tumor node metastasis (TNM) taxonomy classification, stage I refers to the early, non-metastatic stage, while stages II and III usually indicate the intermediate, regional lymphatic metastatic stages, of which stage III has a higher lymphatic metastasis degree than stage II. This correlation may indicate the potential ability of *BACH1* and *VEGFC* to promote cellular migration and cancer invasion. Hence, BACH1 and VEGFC may serve as candidate diagnostic biomarkers in cancer patients.

Figure 8

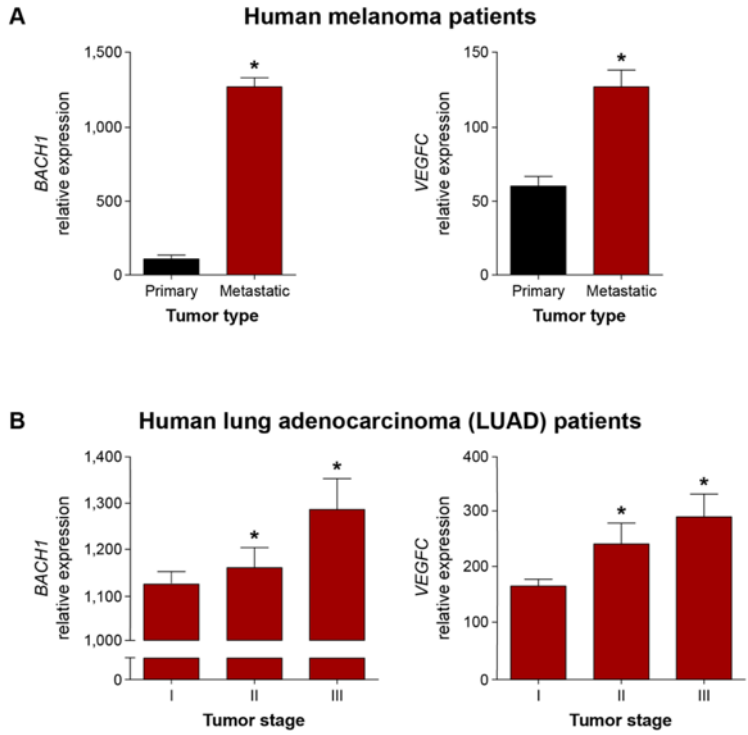

The expression of BACH1 and VEGFC correlates during human cancer progression.

(A) Correlation of *BACH1* and *VEGFC* expression in specimens from melanoma patients clinically diagnosed with a primary tumor (n = 84) in comparison to those with metastatic stage melanoma (n = 356), as deduced from The Cancer Genome Atlas (TCGA) Research Network RNA sequencing (RNA-Seq.) data. Mean ± s.e.m.; *$P \leq 0.0008$. **(B)** Correlation of *BACH1* and *VEGFC* expression in specimens from lung adenocarcinoma (LUAD) clinically diagnosed with primary tumor stages I (n = 292), II (n = 133) and III (n = 95), as analyzed from The Cancer Genome Atlas (TCGA) Research Network RNA-Seq. data. Mean ± s.e.m.; *$P < 0.02$.

Discussion

VEGFC is a potent regulator of the growth and maintenance of blood and lymphatic vessels during embryonic development, tumor expansion and metastasis. The results presented here demonstrate that members of the BACH family regulate VEGFC expression, thereby promoting angiogenesis and lymphangiogenesis during zebrafish development and in ovarian and lung mouse tumor models.

BACH1 and BACH2 are important for the homeostasis of heme, an essential molecule for many biological functions (Igarashi & Watanabe-Matsui, 2014; Warnatz et al., 2011). Imbalanced levels of heme can cause oxidative stress when it reacts with molecular oxygen, which in turn disrupts various cellular signaling pathways. BACH1 was initially discovered as a physiological repressor of heme oxygenease-1 (HO-1), a rate-limiting enzyme in heme

catabolism stimulated by Nuclear factor erythroid 2-related factor 2 (NRF2) (Warnatz et al., 2011). Recent emerging evidence, however, indicate the widespread functions of BACH1 in diverse physiological and pathological settings, including hematopoiesis, inflammation, cardiovascular disease, aging, metabolic disorders and neurodegenerative diseases. BACH2 was established as a crucial factor for B and T cell memory differentiation. Nevertheless, the potential roles of these transcription factors during embryogenesis remain obscure (Sidwell & Kallies, 2016). Members of the BACH family possess both a BTB/POZ and a CNC-bZip functional domain, conferring them with protein-protein interaction and DNA-binding capabilities (Zhou et al., 2016) to the antioxidant response elements (ARE) (Zhou et al., 2016). The BTB/POZ domain, located at the N-terminus, mediates dimer formation (Igarashi & Watanabe-Matsui, 2014). Conversely, the bZip domain enables DNA binding and the formation of heterodimers with small musculoaponeurotic fibrosarcoma (sMaf) transcription factors (Davudian, Mansoori, et al., 2016). Three evolutionary conserved sMafs have been identified in mammals and an additional one in zebrafish, all displaying complex expression patterns during embryogenesis (Yamazaki, Katsuoka, Motohashi, Engel, & Yamamoto, 2012). While single sMaf knockout mice show no or a mild phenotype, triple-knockout embryos display severe growth retardation and liver hypoplasia, resulting in embryonic lethality at E13.5 (Yamazaki et al., 2012). Interestingly, a member of the large Maf family of transcription factors, *mafba* in zebrafish (Koltowska et al., 2015) and *Mafb* in mice (Dieterich et al., 2015), was shown to be activated by VEGFC. In zebrafish, *mafba* is crucial for the migration of lymphatic precursors after their initial sprouting from the cardinal vein (Koltowska et al., 2015). In lymphatic endothelial cells (LECs), MAFB promotes the expression of *PROX1*, *KLF4*, *NR2F2*, and *SOX18,* key transcription factors and markers of differentiated LECs. Furthermore, E14.5 *Mafb*$^{-/-}$ mouse embryos show impaired lymphatic patterning in the skin (Dieterich et al., 2015). Altogether, these studies suggest that the BACH and MAF transcription factor families play key roles during lymphangiogenesis. Uncovering the complexity within these molecular networks may be exploited for the understanding of EC differentiation and vascular development.

Four *bach* genes *(bach1a*, *bach1b*, *bach2a* and *bach2b)* with homology to mammalian BACH are present in the zebrafish genome. Phylogenetic analysis indicates that *bach1a*, *bach1b* and *bach2a*, *bach2b* belong to two distinct groups, *bach1* and *bach2*, respectively, with *bach2* possibly diverging earlier than *bach1* (Luo et al., 2016). It was shown that, during embryogenesis, the two *bach1* genes inhibit heme oxygenase 1a (*hmox1a*) induction

in zebrafish (Fuse et al., 2015). In a recent study, overexpression of *bach1b* was found to suppress developmental angiogenesis by inhibiting Wnt/*β*-catenin signaling (L. Jiang et al., 2017). Herein, we show that the *bach2a* gene controls *vegfc* expression, directing blood and lymphatic vascular development in zebrafish. Yet, the lack of full overlapping expression between *bach2a* and *vegfc* supports additional tissue-specific functions for each of these factors.

Accumulating data establish BACH1 as a critical facilitator of tumorigenesis and metastasis in breast (U. Lee et al., 2013), colon (Davudian, Shajari, et al., 2016), prostate (Shajari et al., 2018) ovarian (Han et al., 2019) and lung (Lignitto et al., 2019; Wiel et al., 2019) cancer. Elevated levels of BACH1 expression have been linked to a higher risk of breast cancer recurrence in patients (Liang et al., 2012), while association with metastatic spread and poorer prognosis has recently been suggested in the case of human ovarian cancer (Han et al., 2019) and lung adenocarcinoma (Lignitto et al., 2019; Wiel et al., 2019). Ectopic expression of *BACH1* in breast cancer cells promotes malignancy and metastasis, while its knockdown suppresses these processes. BACH1 has been placed downstream of the Raf kinase inhibitory protein (RKIP), a tumor suppressor gene shown to inhibit invasion and bone metastasis in a breast cancer xenograft mouse model (U. Lee et al., 2013; Yun et al., 2011). Inactivation of RKIP during tumor expansion results in higher expression of BACH1 and its target genes C-X-C chemokine receptor type 4 (CXCR-4) and matrix metalloproteinase1 (MMP1), established drivers of tumor progression and metastasis (Foley & Kuliopulos, 2014; Mishan, Ahmadiankia, & Bahrami, 2016). Furthermore, ablation of *BACH1* in human colon carcinoma (Davudian, Shajari, et al., 2016) or in prostate cancer cells (Shajari et al., 2018), prevents cell growth, migration and invasion *in vitro*, decreasing the expression of its main metastasis-related genes, MMP1, let-7a and CXCR4. Interestingly, *cxcr4* is expressed in the somites and the endothelium of zebrafish embryos (Chong, Emelyanov, Gong, & Korzh, 2001), where we detect the expression of both *bach2a* and *bach2b* transcripts. *cxcr4* was shown to be crucial for lateral aortae formation (Siekmann, Standley, Fogarty, Wolfe, & Lawson, 2009) and trunk lymphatic vascular network assembly (Cha et al., 2012) and a key modulator of vascular progenitor cells (Sainz & Sata, 2007). In addition to its contribution to development, CXCR4 was shown to play a role in carcinogenesis, tissue repair and other pathological circumstances (Kawaguchi, Zhang, & Nakanishi, 2019). VEGFC can thus be added to a growing list of tumor and metastatic proteins, including CXCR4 and MMP1, all of which are transcriptionally regulated by

BACH1. Including VEGFC as a target of BACH1 allows novel perspectives of the role of BACH1 in vascular development during embryogenesis and pathological conditions. During the past years, a substantial amount of *in vitro*, animal and small-size human studies established BACH proteins as a hub of critical transcriptional networks that govern key processes during normal physiology and disease states. Surprisingly, however, *Bach* single- (Muto et al., 2004; Sun et al., 2002) or double- (Ebina-Shibuya et al., 2016) knockout mice exhibit no phenotype at birth. This may result from the existence of a yet unknown compensatory mechanism similar to the one described here in zebrafish. Further understanding the mechanisms underlying BACH's mode of action during embryogenesis, adult life and tumorigenesis would pave the way to resolving this ambiguity.

Altogether, our results highlight BACH as a novel regulator of angiogenesis and lymphangiogenesis during embryonic development as well as tumor progression. We show that BACH controls the expression of VEGFC, an established pro-lymphangiogenic and angiogenic growth factor. The expanded recognition of BACH1 activity, together with its inhibitory effect on NRF2, an important detoxifying and antioxidant factor, mark it as a potential therapeutic target. Hence, various direct or indirect promising BACH1 modulators have been developed (Arbiser, 2011; Banerjee, Basu, Arbiser, & Pal, 2013; Cuadrado et al., 2019). Accordingly, recent reports demonstrated that targeting of BACH1 and mitochondrial metabolism may serve as an effective therapy for triple negative breast cancer (J. Lee et al., 2019). In two new studies on lung cancer it was shown that therapeutic intervention that either destabilizes BACH1 (Lignitto et al., 2019) or disrupts its ability to induce glycolysis (Wiel et al., 2019) have the potential to inhibit BACH1 pro-metastatic activity. Targeting the BACH1/VEGFC signaling axis with these inhibitors may potentially be significant therapeutically for various blood and lymphatic vessels pathologies as well.

Experimental Procedures

Bioinformatics analysis

Transcription factor binding site analysis was performed using the Genomatix Genome Analyzer (Genomatix Software GmbH, Germany) MatInspector program (Cartharius et al., 2005). Promoter regions of the human, mouse and zebrafish Vegfc genes were extracted from the UCSC genome browser (Kent et al., 2002) as follows: Human-GRC37/hg19 chr4: 177,713,306-177,716,211; Mouse-GRCm38/mm10 chr8:54,075,150-54,077,946; Zebrafish Zv9/danRer7 chr1:39,270,126-39,273,225. The zebrafish *bach* sequences used are: *bach1a*:

NM_001040313; *bach1b*: NM_001020663; *bach2a*: XM_680223 and *bach2b*: XM_677841.

Zebrafish lines and husbandry

The EK and *Tg(fli1:EGFP)*^{y1} (Lawson & Weinstein, 2002) zebrafish lines were maintained under standard conditions (Isogai, Lawson, Torrealday, Horiguchi, & Weinstein, 2003). All experiments were carried out according to the guidelines of the Weizmann Institute Animal Care and Use Committee.

Fluorescence Activated Cell Sorting (FACS) and RT-PCR analysis

Tg(fli1:EGFP)^{y1} embryos at 21-24 hpf and 3 dpf were collected and dissociated as previously described (Nicenboim et al., 2015). FACS of single cell suspensions was performed at 4°C using FACS Aria flow cytometer (Becton Dickinson, San Jose, CA). Total RNA was isolated from equal numbers of GFP^{+} and GFP^{-} cells by PerfectPure RNA Cultured Cell kit (5 PRIME), according to the manufacturer's instructions. RNA (100 ng) from each sample was subjected to first-strand cDNA synthesis with Superscript III reverse transcriptase (Invitrogen) and random hexamers. All PCR conditions were optimized to produce a single product of the correct base pair size in the linear range of the reaction using the following set of primers: *bach1a*: 5'-TGTAAGACGGCGGAGTAAGA and 5'-CTTCAGCTGGTTGTG GTCT, *bach1b*: 5'-CTTCAGTGCTCGTGTGTCCA and 5'-TG TAGGCGAACTCCAGCA AG, *bach2a*: 5'-GACAGAACACGAGCCACTCA and 5'-AC AGCGCATGACATCTTGG A, *bach2b*: 5'-TGCATCCTGAACCTTGAGTGT and 5'-CT GCACATCTCGACACACCT, *fli1*: 5'-CCGAGGTCCTGCTCTCACAT and 5'-GGGAC TGGTCAGCGTGAGAT, *bactin*: 5'-CGAGCAGGAGATGGGAACC and 5'-CAACGG AAACGCTCATTGC.

Construction of the pCS2*vegfc*CDS plasmid

The full-length coding region of zebrafish *vegfc* was amplified from cDNAs derived from 24 hpf embryos using a forward (5'-ATGCACTTATTTGGATTTTCT) and a reverse (5'-TTAGTCCAGTCTTCCCCAG) primers, and sub-cloned into the pCRII-TOPO cloning vector (Invitrogen). Following nucleotide sequence verification, a Gateway-compatible (Invitrogen) middle entry clone was generated using Gateway BP clonase (Invitrogen) mediated recombination. A pCS2*vegfc*CDS plasmid was produced using Gateway LR clonase (Invitrogen). Capped mRNA was transcribed from a Not1-linearised template using

the mMessage mMachine Kit (Ambion).

Microinjection of zebrafish embryos

Morpholino antisense oligonucleotides (Gene Tools) were designed with sequences complementary to zebrafish *bach2a and bach2b* cDNA in a location downstream to the initiating start codon. The morpholino sequences were as follow: *bach2a*: (GenBank accession number XM_680223.4), 5'-TGTCAGGCTTCTCCTCCATAGACAT-3' and *bach2b*: (GenBank accession number XM_677841.2), 5'-CTTCAGACTTCTCATCCA CGGACAT-3'. The morpholino targeting the zebrafish *vegfc* was previously described (Yaniv et al., 2006). As a control the Gene Tools standard control MO (5'-CCTCTTAC CTCAGTTACAATTTATA-3') was applied. Specific Morpholino oligonucleotides were injected into one-cell stage embryos at concentrations from 3.75 up to 10 ng and control MO at 10 ng per embryo. For rescue experiments pCS2*vegfc*CDS mRNA (800 pg per embryo) was simultaneously injected with the morpholino (3.75 ng per embryo). For quantification of the phenotypes, embryos from each group were randomly selected. Quantification was deduced from pools of at least 3 independent experiments.

Design and synthesis of guide RNA (gRNA)

The design of the *bach2a* and *bach2b* CRISPR guide was performed with CHOPCHOP (Montague, Cruz, Gagnon, Church, & Valen, 2014) (chopchop.rc.fas.harvard.edu). Potential off-target sequences were checked using the MIT CRISPR Design site (crispr.mit.edu) (Hsu et al., 2013). Oligonucleotides synthesized for the guide sequence 5'-GGACGTCCTGTGTGACGTGA and 5'-CTGTGCCGAATTCCTGCGCA for *bach2a* and *bach2b* respectively, were cloned into the BsmBI site of the pT7-gRNA plasmid (a gift from Wenbiao Chen) (Addgene plasmid # 46759) (Jao, Wente, & Chen, 2013). Alt-R S.p. Cas9 Nuclease 3NLS (250 ng/µl, Integrated DNA Technologies) and gRNA (125 ng/µl) in 5 µl total volume were co-injected into one-cell-stage *Tg(fli1:EGFP)*^{y1} embryos. To detect mutagenic events, DNA was extracted from 24 hpf embryos, amplified using a set of primers 5'-AGCAAGGAATGTCTATGGAGGA and 5'-ATGAGTGGCTCGTGT TCTGTC (235bp) for *bach2a* and 5'-CGCTCCATTGTT ACAGTTTGC and 5'- GCCG TCCTCTTCACTGCGC (157 bp) for *bach2b*. PCR products were separated on 3.5% MetaPhor Agarose gel (Lonza). When both genotyping and phenotypic analyses of single zebrafish embryos from heterozygous *bach2a* intercross was needed, the larval tail (6 dpf)

was used for genotyping, whereas RNA was extracted from the anterior part using NucleoSpin RNA plus XS RNA purification kit (Macherey-Nagel).

Whole-mount *in situ* Hybridization

Embryos were dechorionated and fixed overnight in 4% PFA at 4°C, at the appropriate time points. *In situ* hybridization was performed as previously described (Yaniv et al., 2006) using single-stranded digoxygenin-dUTP-labeled RNA probes transcribed by T7 RNA polymerase (Roche). The PCR generated probes were amplified with the following set of primers: *bach2a*: 5'-AAGAGTGAGCTAGAGGGCA and 5'-CGTTCTCTTGTTCGGG ATCTTG; *bach2b*: 5'-CTGCGCAGTGAAGAGGACGG and 5'-GCTCCACCTCTTGC TTGCAC; *vegfc*: 5'-CATCAGCACTTCATACATCAGC and 5'-GTCCAGTCTTCCCC AGTATG; *lyve1*: 5'-GGTTTGGTTGGGTTGAGGAGC and 5'-TTAGGAAGAGTCAG AGTCTTGTTC; *flt4*: 5'-CTCGAGAATGACATGTGCTGG and 5'-CAGCCAGCGAG CACAAAGC. After performance of a color reaction with alkaline phosphatase substrates (Roche), embryos were fixed in 4% PFA and washed in PBS supplemented with 0.1% Tween-20 (PBST). For tissue clarification embryos were mounted in glycerol and imaged using Leica M165 FC stereomicroscope.

Cell culture

Human ovarian clear cell carcinoma ES2 cell line (American Type Culture Collection) was cultured in DMEM supplemented with 10% fetal bovine serum (FBS). Mouse D122 Lewis lung carcinoma cell line (Eisenbach et al., 1984), kindly provided by Prof. Lea Eisenbach, Weizmann Institute of Science, Israel) was grown in DMEM containing 10% FBS, 1 mM sodium pyruvate and 1% nonessential amino acids. All cell lines were routinely tested for mycoplasma contamination using the EZ-PCR Mycoplasma Test Kit (Biological Industries).

Establishment of stable BACH1-overexpressing cell pools

Full-length coding region of the human BACH1 (*BACH1*, GenBank accession number NM_206866) and mouse Bach1 (*Bach1*, GenBank accession number BC057894.1) with an *N*-terminal hemagglutinin (HA) tag were reverse transcribed with SuperScript III Reverse Transcriptase (Invitrogen) and PCR-amplified using Phusion high-fidelity DNA polymerase (New England Biolabs) together with the following set of primers: *BACH1*: 5'-ATGTCTCTGAGTGAGAACTCGG and 5'-TTACTCATCAGTAGTACATTTATC;

Bach1: 5'-ATGTCTGTGAGTGAGAGTGCG and 5'-TTACTCGTCAGTAGTGCACTTG. The fragments were ligated into pCRII-TOPO and their sequence fidelity was confirmed by sequencing. Inserts were restricted and ligated into pEIRES expression vector containing the human EF-1a promoter (Hobbs, Jitrapakdee, & Wallace, 1998) to produce the pIRES*BACH*1 and pIRES*Bach1* constructs. ES2 and D122 cells were transfected with pIRES*BACH1* and pIRES*Bach1* expression vectors respectively, using Lipofectamine 2000 reagent (Invitrogen) and selected with 2.5µg/ml puromycin (Sigma) as was previously described (Cohen et al., 2009). An average of 50 individual puromycin-resistant colonies were collected together and BACH1-overexpression was confirmed by immunoblotting. ES2 and D122 cells that were stably transfected with the pEIRES empty vector were used as controls.

Chromatin immunoprecipitation (ChIP) assay

The ChIP experiments were performed using the ChIP-IT-Express kit (Active Motif catalog no. 53009). Cells were fixed and cross-linked using 1% formaldehyde at room temperature for 10 min. Fixation was stopped by adding glycine. DNA extracted from nuclear fraction was subjected to enzymatic shearing for 35 min at 37°C to obtain mononucleosomes. The resulting chromatin preparation was immunoprecipitated with magnetic protein G coupled beads and 10 mg of either anti HA-tag (HA.11, Covance), Bach1 (Santa Cruz, sc-14700) or nonspecific-IgG antibody. DNA-protein crosslinking was reversed at 65°C (4 h), treated with Proteinase K (2 h, 42°C). The recovered DNA was then subjected to PCR using the following set of specific primers: *BACH* proximal site: 5'-GAGGGAGAGTGAGAGGGG and 5'-CGCAGGATCCTCCAGAGC; *BACH* distal site: 5'-CCGAGTCTGATGGGATGG AA and 5'-GCCTTTGTTGATACAGCCTTGG.

Transient transfection and Luciferase Assay

The 5′-regulatory region of human VEGFC gene (NG_034216.1) encompassing 2274 nucleotides (-1 to -2274 in relation to ATG, Figure 1) was synthesized by GenScript. This fragment was then used as a template for deletion of either the proximal (nt -623 to -603, 5'-GGCGCGTCAGTCATGCCCTGC) or distal (nt -2074 to -2054, 5'-GTAGTGTGAGTCAA CACTGTG) BACH binding site individually or in combination. Subsequently, these synthesized fragments were sub-cloned into the pGL4.10[*luc2*] promoter-less vector (Promega) between KpnI and XhoI restriction sites to generate the pVEGFCwt-Luc (wild-type VEGFC promoter region), pVEGFCΔPro-Luc (VEGFC promoter region deleted of the

proximal BACH binding site), pVEGFCΔDis-Luc (VEGFC promoter region deleted of the distal BACH binding site) and pVEGFCΔProDis-Luc (VEGFC promoter region deleted of both proximal and distal BACH binding sites). All constructs were verified by DNA sequence analysis. For the luciferase reporter gene assay, ES2 cells plated in 24-well plates (40,000 cells per well) were co-transfected with the indicated pVEGFC-Luc construct in combination with the pRL-TK-Renilla (pRL-TK vector, Promega) luciferase internal control vector using Lipofectamine 2000 (Thermo Fisher Scientific), according to the manufacturer's instructions. After 48 h cells were lysed and luciferase activity was measured using the Dual-Luciferase Assay System (Promega). All luciferase data were corrected for transfection efficiency based on the Renilla internal control following by subtraction of the pGL4.10[*luc2*] activity background. The data were calculated as means ± standard error of three independent experiments, each performed in nine replications. Luciferase activities for each transfection are plotted as average fold-change in relation to the pVEGFCwt-Luc.

Western blot analysis

Protein extraction was performed in RIPA buffer (20 mM Tris, pH 7.4, 137 mM NaCl, 10% glycerol, 0.5% (wt/vol) sodium deoxycholate, 0.1% (wt/vol) sodium dodecyl sulfate (SDS), 1% Triton X-100, 2 mM EDTA) supplemented with 1 mM phenylmethylsulfonyl fluoride (PMSF) and protease inhibitor cocktail (Sigma). Lysates (20 μg/lane) were electrophoresed in SDS-PAGE under reducing conditions and transferred to a nitrocellulose (Whatman). Membranes were probed with anti HA-tag monoclonal antibody (Covance, HA.11, 1:100) while β-Tubulin (Santa Cruz, H-235, 1: 500) was used as a loading control. Appropriate HRP-conjugated anti-mouse or anti-rabbit secondary antibodies (Jackson ImmunoResearch, 1:10,000) were used respectively.

Cell invasion assay

The invasion potential of the cells was examined *in vitro* using BioCoat Matrigel Invasion Chamber (Corning). A total of $80x10^3$ cells suspended in serum-free medium were seeded in the upper chamber. To initiate cell invasion medium supplemented with 10% FBS was added as a chemoattractant in the low chamber. Cells were incubated at 37°C for 20 h and invaded cells on the inferior surface of the inserts were fixed, washed, and stained with crystal violet (Sigma). Each assay was repeated two times in duplicates. For analysis the entire Matrigel surface area was imaged (Olympus SZX16 stereomicroscope,

2.5×magnification) and quantified using the ImageJ software. To ensure that the difference in invasion rate is not due to differential cell growth rate, total cell number validation was carried on a parallel plate. Cells were stained with crystal violet, lysed with 1% SDS, 0.1N NaOH solution followed by direct dye intensity measurement.

Tumor initiation, histologic preparation, immunohistochemistry and morphometric analysis

Subcutaneous tumors were generated by injecting 2×10^6 single-cell suspensions of cells in 100 µl PBS into a shaved lower right flank of seven-week old mice. D122 Control or *Bach1*- overexpressing cells were injected to male immunocompetent syngeneic C57BL/6 (Harlan Laboratories), whereas ES2 cells were injected to female immunodeficient CD1 nude (Harlan Laboratories) mice. Orthotopic metastatic tumor growth was initiated by injecting 1×10^6 ES2 cells intraperitoneally at a remote site in the abdomen of seven-week-old female CD1 nude mice (Harlan Laboratories). In all experiments, animals were randomly assigned to the control and overexpressing cells injected groups. Excised mouse tumors were rinsed in ice-cold PBS and then gradually fixed at 4°C in 2.5% and 1% PFA for 24 and 48 hours, respectively. Paraffin-embedded tissue was sectioned serially at 4µm thickness. The first slide was stained with hematoxylin and eosin, whereas other representative slides underwent immunohistochemical staining using the following antibodies: anti CD34 (Cedarlane Laboratories, 1:100), LYVE1 (Fitzgerald Industries, 1:100), cytokeratin 7 (Abcam, ab9021, 1:200) and VEGFC (Santa Cruz, H-190 1:200). Morphometric blood and lymphatic vessel coverage analysis were performed on CD-34 and LYVE1 stained tumor sections, respectively. Images of CD-34-stained sections were captured with a fluorescence microscope (NI-U, Nikon, Tokyo, Japan), equipped with Plan Fluor objectives connected to CCD camera (DS-Ri1, Nikon). Digital images were collected and assembled using Adobe Photoshop (Adobe Systems). LYVE1 immunohistochemical-stained sections were scanned using the Panoramic Viewer. The density of vessels was evaluated using Image Pro Plus software (Media Cybernetics). For all analysis, investigators were blinded and unaware of group allocation. All animal experiments described in this study were performed according to the Guidelines the Weizmann Institute Animal Care and Use Committee. For immunostaining of ES2 cells, fixation was carried out in 4% paraformaldehyde for 10 minutes. Fixed cells were then blocked for unspecific staining in 0.3% Triton X-100, 10% horse serum for 90 min at RT, incubated with antibodies directed either against HA-tag (Sigma, 1:200) or VEGFC (Santa Cruz, H-190

1:200)) antibody for 2 h at room temperature and visualized by incubating the cells with goat anti-rabbit Cy3 (Jackson ImmunoResearch, 1:10,000) secondary antibody. Nuclei were counterstained with DAPI (Invitrogen).

Quantitative Real-Time-PCR (qRT-PCR)

Total RNA was isolated from cultured cells or tumor specimens by PerfectPure RNA Cultured Cell or Tissue kit (5 PRIME) respectively, according to the manufacturer's instructions. RNA (1 μg) from each sample was subjected to first-strand cDNA synthesis with the High-Capacity cDNA Reverse Transcription kit (Applied Biosystems) and random hexamers. Quantitative real-time PCR was conducted with LightCycler-FastStart DNA Master SYBR Green I kit (Roche) using a LightCycler 480 Real-Time PCR System (Roche). The relative expression level of each target gene was determined using glyceraldehyde-3 phosphate dehydrogenase (GAPDH) and beta-2-microglobulin (B2M) as reference genes. Primers used were as follows: human *BACH1*: 5'-TCTTCCAGAAG AGGTGACAGT and 5'-ACTCCACACATTTGCACACT; *VEGFA: 5'*-ATGCGGATC AAACCTCACC and 5'-T CTTTCTTTGGTCTGCATTCAC; *VEGFB:5'*- CCACCAG AGGAAAGTGGTGTC *and 5'*- ACAGCGCTGCACAGTCAC; *VEGFC*: 5'-GCCACGG CTTATGCAAGCAAAGAT and 5'-AGTTGAGGTTGGCCTGTTCTCTGT; *MMP1*: 5'-CTGGCCACAACTGCCAAATG and 5'-CTGTCCCTGAACAGCCCAGTACTTA; *GAPDH*: 5'-AGGGCTGCTTTTAACTCTGGT and 5'-CCCCACTTGATTTTGGAG GGA; *B2M*: 5'-TTCTGGCCTGGAGGCTATC and 5'-TCAGGAAATTTGACTTTC CATTC; Mouse *Bach1*: 5'-TGACAGCGAGTC CTGTTCTG and 5'-TTATCCGTTGG GCATTGAA; *Vegfa*: 5'-TCTTCAAGCCATCCTGTGTG *and 5'*-GAGGTTTGATCCGC ATAATCTG; *Vegfb*: 5'-ACGATGGCCTGGAATGTGTG and 5'-TGGTCTGCATTCA CATTGGC; *Vegfc*: 5'- GTAAAAACAAACTTTTCCCTAATTC and 5'-TTTAAGGA AGCACTTCTGTGTGT; *Vegfa*: 5'- TCTTCAAGCCATCCTGTGTG and *5'*-GAGGTTT GATCCGCATAATCTG; *Vegfb*: 5'-ACGATGGCCTGGAATGTGTG and 5'-TGGTCTG CATTCACATTGGC; *Gapdh*: 5'-GACGGCCGCATCTTCTTGTG and 5'-CTTCCCATT CTCGGCCTTGACTGT; *B2m*: 5'-CC CGCCTCACATTGAAATCC and 5'- GCGTATG TATCAGTCTCAGTGG. Zebrafish *bach2b*; 5'-CAGCATGCCAGAGGAGGT and 5'-A GTGATTGCTCTCCGACGC; *bactin* 5'-TGACAGGATGCAGAAGGAGA and 5'- GCC TCCGATCCAGACAGAGT.

Clearing and immunofluorescence staining

Excised tumors were fixed with 4% PFA for 1 week at 4°C, washed three times with phosphate-buffered saline (PBS), permeabilized with (0.2% Triton X-100 in PBS) for 4 h, and immersed overnight in blocking solution (PBS containing 0.05% Triton X-100 and 10% normal goat serum). For immunofluorescent staining tumors were incubated with primary mouse anti LYVE1 antibody (Fitzgerald Industries) diluted (1:250) in an antibody cocktail (50% blocking solution, 0.05% Triton X-100 in PBSX1) for 1week at 4°C, washed 24 h (1% blocking solution, 0.05% Triton X-100 in PBS), and probed with an Alexa fluor-594 conjugated goat anti rabbit secondary antibody (Molecular Probes - Life Technologies, A11037, 1: 250) diluted in antibody cocktail for an additional week at 4°C. Following 24 h wash, tumors were subjected to a Whole Organ Blood and Lymphatic Vessels Imaging (WOBLI) clearing procedure (K. Chung et al., 2013; Hama et al., 2011; Oren et al., 2018). Briefly, tumors were re-fixed with 4% PFA for 24-72h at 4°C, transferred to hydrogel solution (4% Acrylamide, 0.025% Bisacrylamide, 0.25% Va-044 and 4% PFA in PBS) for 1week and passively cleared (200 mM Boric acid and 4% SDS) for 2 weeks at 37°C. Subsequently, tumors were placed in Scale solution (4M Urea, 10% Glycerol and 0.1% Triton X-100) for 48 h. A sequence of 3D images and movies were acquired using Zeiss LSM710 confocal microscope (Zeiss, Oberkochen, Germany).

Microscopy

Images were acquired on Zeiss LSM 780 upright confocal microscope (Carl Zeiss) with a W-Plan Apochromat ×20 objective, NA 1.0. Fluorescent proteins were excited with single-photon laser (488nm). Alternatively, Leica TCS SP8 microscope, equipped with environmental control, 2 internal Hybrid (HyD) detectors and Acusto Optical Tunable Filter (Leica microsystems CMS GmbH, Germany) was used and excitation was done by using 488nm by Ar laser and emission was collected using the internal HyD detector at 510-625nm with gain of 100.

Statistical Analysis

Statistical analyses were performed with analytic computerized software (Statistix 8 Student Edition, Analytical Software, Tallahassee, FL, USA). Comparisons between treatment groups were performed with either ANOVA or Kruskal–Wallis nonparametric ANOVA (alternatively, t-test or Wilcoxon Rank Sum Test were used if only two groups were compared, respectively). ANOVA test was used to analyze normally distributed data

(evaluated by Shapiro–Wilk test) that had equal variances between groups (evaluated by Bartlett's test), whereas Kruskal–Wallis nonparametric ANOVA was used to analyze data that were not normally distributed and/or had unequal variance between groups; when relevant, Tukey HSD test, or Mean Ranks test, respectively, were used for All-Pairwise Comparisons. Fisher's exact test analysis was used to compare proportional data. Differences were considered significant at $P < 0.05$. Unless otherwise noted, data are presented as mean ± s.e.m.

Acknowledgments

The authors would like to thank Irit Orr and Ron Rotkopf for assistance with human cancer data analysis; Prof. Eytan Domany and Dr. Noa Ben-Moshe for transcription factor analysis; Ayala Sharp for FACS analysis support; Michal Shemesh for assisting with imaging requirements; Ofir Atrakchi, Yona Ely, Ron Hadas, Tal Lupo and Gila Meir for technical assistance; Noa David for graphic design; Prof. Lea Eisenbach for providing the mouse D122 Lewis lung carcinoma cell line; Gabriella Almog, Ala Glozman and Roy Hofi for fish care; and Beni Siani and Alon Harmelin for animal care.

This work was supported in part by Israel Science Foundation grants 326/14 (to MN and BC), 748/2009 (to KY) and 861/2013 (to KY); European Research Council Advanced grant 232640-IMAGO (to MN) and Starting grant 335605 (to KY), the Thompson Foundation (to MN), National Institutes of Health grant (R01 CA75334, to MN), Marie Curie Actions-International Reintegration grants FP7-PEOPLE-2009-RG 256393 (to KY), the H&M Kimmel Institute for Stem Cell Research (to KY), and the Estate of Emile Mimran (SABRA program) (to KY). Michal Neeman is the incumbent of the Helen and Morris Mauerberger Chair in Biological Sciences. K.Y. is supported by the Willner Family Center for Vascular Biology; the estate of Paul Ourieff; the Carolito Stiftung; Lois Rosen, Los Angeles, CA; Edith Frumin; the Fondazione Henry Krenter; the Wallach Hanna& Georges Lustgarten Fund; and the Polen Charitable Trust.

References

Alvarez, A., & Woolf, P. J. (2011). RegNetB: predicting relevant regulator-gene relationships in localized prostate tumor samples. *BMC Bioinformatics, 12*, 243. doi:10.1186/1471-2105-12-243

Arbiser, J. L. (2011). Fumarate esters as angiogenesis inhibitors: key to action in psoriasis? *J Invest Dermatol, 131*(6), 1189-1191. doi:10.1038/jid.2011.45

Baluk, P., Tammela, T., Ator, E., Lyubynska, N., Achen, M. G., Hicklin, D. J., . . . McDonald, D. M. (2005). Pathogenesis of persistent lymphatic vessel hyperplasia in chronic airway inflammation. *J Clin Invest, 115*(2), 247-257. doi:10.1172/JCI22037

Banerjee, P., Basu, A., Arbiser, J. L., & Pal, S. (2013). The natural product honokiol inhibits calcineurin inhibitor-induced and Ras-mediated tumor promoting pathways. *Cancer Lett, 338*(2), 292-299. doi:10.1016/j.canlet.2013.05.036

Cartharius, K., Frech, K., Grote, K., Klocke, B., Haltmeier, M., Klingenhoff, A., . . . Werner, T. (2005). MatInspector and beyond: promoter analysis based on transcription factor binding sites. *Bioinformatics, 21*(13), 2933-2942. doi:10.1093/bioinformatics/bti473

Cha, Y. R., Fujita, M., Butler, M., Isogai, S., Kochhan, E., Siekmann, A. F., & Weinstein, B. M. (2012). Chemokine signaling directs trunk lymphatic network formation along the preexisting blood vasculature. *Dev Cell, 22*(4), 824-836. doi:10.1016/j.devcel.2012.01.011

Chen, H. I., Sharma, B., Akerberg, B. N., Numi, H. J., Kivela, R., Saharinen, P., . . . Red-Horse, K. (2014). The sinus venosus contributes to coronary vasculature through VEGFC-stimulated angiogenesis. *Development, 141*(23), 4500-4512. doi:10.1242/dev.113639

Chen, J. C., Chang, Y. W., Hong, C. C., Yu, Y. H., & Su, J. L. (2012). The role of the VEGF-C/VEGFRs axis in tumor progression and therapy. *Int J Mol Sci, 14*(1), 88-107. doi:10.3390/ijms14010088

Chen, Y., Wang, D., Peng, H., Chen, X., Han, X., Yu, J., . . . Li, F. (2019). Epigenetically upregulated oncoprotein PLCE1 drives esophageal carcinoma angiogenesis and proliferation via activating the PI-PLCepsilon-NF-kappaB signaling pathway and VEGF-C/ Bcl-2 expression. *Mol Cancer, 18*(1), 1. doi:10.1186/s12943-018-0930-x

Chong, S. W., Emelyanov, A., Gong, Z., & Korzh, V. (2001). Expression pattern of two zebrafish genes, cxcr4a and cxcr4b. *Mech Dev, 109*(2), 347-354.

Chung, A. S., & Ferrara, N. (2011). Developmental and pathological angiogenesis. *Annu Rev Cell Dev Biol, 27*, 563-584. doi:10.1146/annurev-cellbio-092910-154002

Chung, K., Wallace, J., Kim, S. Y., Kalyanasundaram, S., Andalman, A. S., Davidson, T. J., . . . Deisseroth, K. (2013). Structural and molecular interrogation of intact biological systems. *Nature, 497*(7449), 332-337. doi:10.1038/nature12107

Cohen, B., Addadi, Y., Sapoznik, S., Meir, G., Kalchenko, V., Harmelin, A., . . . Neeman, M. (2009). Transcriptional regulation of vascular endothelial growth factor C by oxidative and thermal stress is mediated by lens epithelium-derived growth factor/p75. *Neoplasia, 11*(9), 921-933.

Covassin, L., Amigo, J. D., Suzuki, K., Teplyuk, V., Straubhaar, J., & Lawson, N. D. (2006). Global analysis of hematopoietic and vascular endothelial gene expression by tissue specific microarray profiling in zebrafish. *Dev Biol, 299*(2), 551-562. doi:10.1016/j.ydbio.2006.08.020

Covassin, L. D., Villefranc, J. A., Kacergis, M. C., Weinstein, B. M., & Lawson, N. D. (2006). Distinct genetic interactions between multiple Vegf receptors are required for development of different blood vessel types in zebrafish. *Proc Natl Acad Sci U S A, 103*(17), 6554-6559. doi:10.1073/pnas.0506886103

Cuadrado, A., Rojo, A. I., Wells, G., Hayes, J. D., Cousin, S. P., Rumsey, W. L., . . . Dinkova-Kostova, A. T. (2019). Therapeutic targeting of the NRF2 and KEAP1 partnership in chronic diseases. *Nat Rev Drug Discov, 18*(4), 295-317. doi:10.1038/s41573-018-0008-x

Davudian, S., Mansoori, B., Shajari, N., Mohammadi, A., & Baradaran, B. (2016). BACH1, the master regulator gene: A novel candidate target for cancer therapy. *Gene, 588*(1), 30-37. doi:10.1016/j.gene.2016.04.040

Davudian, S., Shajari, N., Kazemi, T., Mansoori, B., Salehi, S., Mohammadi, A., . . . Baradaran, B. (2016). BACH1 silencing by siRNA inhibits migration of HT-29 colon cancer cells through reduction of metastasis-related genes. *Biomed Pharmacother, 84*, 191-198. doi:10.1016/j.biopha.2016.09.021

Dieterich, L. C., Klein, S., Mathelier, A., Sliwa-Primorac, A., Ma, Q., Hong, Y. K., . . . Detmar, M. (2015). DeepCAGE Transcriptomics Reveal an Important Role of the Transcription Factor MAFB in the Lymphatic Endothelium. *Cell Rep, 13*(7), 1493-1504. doi:10.1016/j.celrep.2015.10.002

Ebina-Shibuya, R., Watanabe-Matsui, M., Matsumoto, M., Itoh-Nakadai, A., Funayama, R., Nakayama, K., . . . Igarashi, K. (2016). The double knockout of Bach1 and Bach2 in mice reveals shared compensatory mechanisms in regulating alveolar macrophage function and lung surfactant homeostasis. *J Biochem*. doi:10.1093/jb/mvw041

Eisenbach, L., Hollander, N., Greenfeld, L., Yakor, H., Segal, S., & Feldman, M. (1984). The differential expression of H-2K versus H-2D antigens, distinguishing high-metastatic from low-metastatic clones, is correlated with the immunogenic properties of the tumor cells. *Int J Cancer, 34*(4), 567-573.

El-Brolosy, M. A., Kontarakis, Z., Rossi, A., Kuenne, C., Gunther, S., Fukuda, N., . . . Stainier, D. Y. R. (2019). Genetic compensation triggered by mutant mRNA degradation. *Nature, 568*(7751), 193-197. doi:10.1038/s41586-019-1064-z

El-Brolosy, M. A., & Stainier, D. Y. R. (2017). Genetic compensation: A phenomenon in search of mechanisms. *PLoS Genet, 13*(7), e1006780. doi:10.1371/journal.pgen.1006780

Foley, C. J., & Kuliopulos, A. (2014). Mouse matrix metalloprotease-1a (Mmp1a) gives new insight into MMP function. *J Cell Physiol, 229*(12), 1875-1880. doi:10.1002/jcp.24650

Fuse, Y., Nakajima, H., Nakajima-Takagi, Y., Nakajima, O., & Kobayashi, M. (2015). Heme-mediated inhibition of Bach1 regulates the liver specificity and transience of the Nrf2-dependent induction of zebrafish heme oxygenase 1. *Genes Cells, 20*(7), 590-600. doi:10.1111/gtc.12249

Gauvrit, S., Villasenor, A., Strilic, B., Kitchen, P., Collins, M. M., Marin-Juez, R., . . . Stainier, D. Y. R. (2018). HHEX is a transcriptional regulator of the VEGFC/FLT4/PROX1 signaling axis during vascular development. *Nat Commun, 9*(1), 2704. doi:10.1038/s41467-018-05039-1

Glinsky, G. V., Glinskii, A. B., Stephenson, A. J., Hoffman, R. M., & Gerald, W. L. (2004). Gene expression profiling predicts clinical outcome of prostate cancer. *J Clin Invest, 113*(6), 913-923. doi:10.1172/JCI20032

Gore, A. V., Swift, M. R., Cha, Y. R., Lo, B., McKinney, M. C., Li, W., . . . Weinstein, B. M. (2011). Rspo1/Wnt signaling promotes angiogenesis via Vegfc/Vegfr3. *Development, 138*(22), 4875-4886. doi:10.1242/dev.068460

Hama, H., Kurokawa, H., Kawano, H., Ando, R., Shimogori, T., Noda, H., . . . Miyawaki, A. (2011). Scale: a chemical approach for fluorescence imaging and reconstruction of transparent mouse brain. *Nat Neurosci, 14*(11), 1481-1488. doi:10.1038/nn.2928

Han, W., Zhang, Y., Niu, C., Guo, J., Li, J., Wei, X., . . . Meng, D. (2019). BTB and CNC homology 1 (Bach1) promotes human ovarian cancer cell metastasis by HMGA2-mediated epithelial-mesenchymal transition. *Cancer Lett*. doi:10.1016/j.canlet.2019.01.003

Helker, C. S., Schuermann, A., Karpanen, T., Zeuschner, D., Belting, H. G., Affolter, M., . . . Herzog, W. (2013). The zebrafish common cardinal veins develop by a novel mechanism: lumen ensheathment. *Development, 140*(13), 2776-2786. doi:10.1242/dev.091876

Hobbs, S., Jitrapakdee, S., & Wallace, J. C. (1998). Development of a bicistronic vector driven by the human polypeptide chain elongation factor 1alpha promoter for creation of stable mammalian cell lines that express very high levels of recombinant proteins. *Biochem Biophys Res Commun, 252*(2), 368-372. doi:10.1006/bbrc.1998.9646

Hogan, B. M., Bos, F. L., Bussmann, J., Witte, M., Chi, N. C., Duckers, H. J., & Schulte-Merker, S. (2009). Ccbe1 is required for embryonic lymphangiogenesis and venous sprouting. *Nat Genet, 41*(4), 396-398. doi:10.1038/ng.321

Hogan, B. M., Herpers, R., Witte, M., Helotera, H., Alitalo, K., Duckers, H. J., & Schulte-Merker, S. (2009). Vegfc/Flt4 signalling is suppressed by Dll4 in developing zebrafish intersegmental arteries. *Development, 136*(23), 4001-4009. doi:10.1242/dev.039990

Hsu, P. D., Scott, D. A., Weinstein, J. A., Ran, F. A., Konermann, S., Agarwala, V., . . . Zhang, F. (2013). DNA targeting specificity of RNA-guided Cas9 nucleases. *Nat Biotechnol, 31*(9), 827-832. doi:10.1038/nbt.2647

Igarashi, K., & Watanabe-Matsui, M. (2014). Wearing red for signaling: the heme-bach axis in heme metabolism, oxidative stress response and iron immunology. *Tohoku J Exp Med, 232*(4), 229-253.

Isogai, S., Lawson, N. D., Torrealday, S., Horiguchi, M., & Weinstein, B. M. (2003). Angiogenic network formation in the developing vertebrate trunk. *Development, 130*(21), 5281-5290. doi:10.1242/dev.00733

Jao, L. E., Wente, S. R., & Chen, W. (2013). Efficient multiplex biallelic zebrafish genome editing using a CRISPR nuclease system. *Proc Natl Acad Sci U S A, 110*(34), 13904-13909. doi:10.1073/pnas.1308335110

Jiang, H., Shao, W., & Zhao, W. (2014). VEGF-C in non-small cell lung cancer: meta-analysis. *Clin Chim Acta, 427*, 94-99. doi:10.1016/j.cca.2013.10.002

Jiang, L., Yin, M., Xu, J., Jia, M., Sun, S., Wang, X., . . . Meng, D. (2017). The Transcription Factor Bach1 Suppresses the Developmental Angiogenesis of Zebrafish. *Oxid Med Cell Longev, 2017*, 2143875. doi:10.1155/2017/2143875

Karaman, S., Hollmen, M., Robciuc, M. R., Alitalo, A., Nurmi, H., Morf, B., . . . Detmar, M. (2015). Blockade of VEGF-C and VEGF-D modulates adipose tissue inflammation and improves metabolic parameters under high-fat diet. *Mol Metab, 4*(2), 93-105. doi:10.1016/j.molmet.2014.11.006

Karkkainen, M. J., Haiko, P., Sainio, K., Partanen, J., Taipale, J., Petrova, T. V., . . . Alitalo, K. (2004). Vascular endothelial growth factor C is required for sprouting of the first lymphatic vessels from embryonic veins. *Nat Immunol, 5*(1), 74-80. doi:10.1038/ni1013

Kawaguchi, N., Zhang, T. T., & Nakanishi, T. (2019). Involvement of CXCR4 in Normal and Abnormal Development. *Cells, 8*(2). doi:10.3390/cells8020185

Kent, W. J., Sugnet, C. W., Furey, T. S., Roskin, K. M., Pringle, T. H., Zahler, A. M., & Haussler, D. (2002). The human genome browser at UCSC. *Genome Res, 12*(6), 996-1006. doi:10.1101/gr.229102. Article published online before print in May 2002

Khromova, N., Kopnin, P., Rybko, V., & Kopnin, B. P. (2012). Downregulation of VEGF-C expression in lung and colon cancer cells decelerates tumor growth and inhibits metastasis via multiple mechanisms. *Oncogene, 31*(11), 1389-1397. doi:10.1038/onc.2011.330

Kodama, M., Kitadai, Y., Tanaka, M., Kuwai, T., Tanaka, S., Oue, N., . . . Chayama, K. (2008). Vascular endothelial growth factor C stimulates progression of human gastric cancer via both autocrine and paracrine mechanisms. *Clin Cancer Res, 14*(22), 7205-7214. doi:10.1158/1078-0432.CCR-08-0818

Koltowska, K., Paterson, S., Bower, N. I., Baillie, G. J., Lagendijk, A. K., Astin, J. W., . . . Hogan, B. M. (2015). mafba is a downstream transcriptional effector of Vegfc signaling essential for embryonic lymphangiogenesis in zebrafish. *Genes Dev, 29*(15), 1618-1630. doi:10.1101/gad.263210.115

Kuchler, A. M., Gjini, E., Peterson-Maduro, J., Cancilla, B., Wolburg, H., & Schulte-Merker, S. (2006). Development of the zebrafish lymphatic system requires VEGFC signaling. *Curr Biol, 16*(12), 1244-1248. doi:10.1016/j.cub.2006.05.026

Lal, N., Puri, K., & Rodrigues, B. (2018). Vascular Endothelial Growth Factor B and Its Signaling. *Front Cardiovasc Med, 5*, 39. doi:10.3389/fcvm.2018.00039

Lawson, N. D., & Weinstein, B. M. (2002). In vivo imaging of embryonic vascular development using transgenic zebrafish. *Dev Biol, 248*(2), 307-318.

Lee, J., Lee, J., Farquhar, K. S., Yun, J., Frankenberger, C. A., Bevilacqua, E., . . . Rosner, M. R. (2014). Network of mutually repressive metastasis regulators can promote cell heterogeneity and metastatic transitions. *Proc Natl Acad Sci U S A, 111*(3), E364-373. doi:10.1073/pnas.1304840111

Lee, J., Yesilkanal, A. E., Wynne, J. P., Frankenberger, C., Liu, J., Yan, J., . . . Rosner, M. R. (2019). Effective breast cancer combination therapy targeting BACH1 and mitochondrial metabolism. *Nature, 568*(7751), 254-258. doi:10.1038/s41586-019-1005-x

Lee, U., Frankenberger, C., Yun, J., Bevilacqua, E., Caldas, C., Chin, S. F., . . . Rosner, M. R. (2013). A prognostic gene signature for metastasis-free survival of triple negative breast cancer patients. *PLoS One, 8*(12), e82125. doi:10.1371/journal.pone.0082125

Liang, Y., Wu, H., Lei, R., Chong, R. A., Wei, Y., Lu, X., . . . Kang, Y. (2012). Transcriptional network analysis identifies BACH1 as a master regulator of breast cancer bone metastasis. *J Biol Chem, 287*(40), 33533-33544. doi:10.1074/jbc.M112.392332

Lignitto, L., LeBoeuf, S. E., Homer, H., Jiang, S., Askenazi, M., Karakousi, T. R., . . . Pagano, M. (2019). Nrf2 Activation Promotes Lung Cancer Metastasis by Inhibiting the Degradation of Bach1. *Cell, 178*(2), 316-329.e318. doi:10.1016/j.cell.2019.06.003

Lohela, M., Bry, M., Tammela, T., & Alitalo, K. (2009). VEGFs and receptors involved in angiogenesis versus lymphangiogenesis. *Curr Opin Cell Biol, 21*(2), 154-165. doi:10.1016/j.ceb.2008.12.012

Lohela, M., Helotera, H., Haiko, P., Dumont, D. J., & Alitalo, K. (2008). Transgenic induction of vascular endothelial growth factor-C is strongly angiogenic in mouse embryos but leads to persistent lymphatic hyperplasia in adult tissues. *Am J Pathol, 173*(6), 1891-1901. doi:10.2353/ajpath.2008.080378

Luo, Q., Wu, C., Sun, S., Lu, F., Xie, L., Zhao, H., . . . Zhou, Q. (2016). The spatial-temporal expression and functional divergence of bach homologs in zebrafish Danio rerio. *J Fish Biol, 88*(4), 1584-1597. doi:10.1111/jfb.12931

Ma, Q., Dieterich, L. C., Ikenberg, K., Bachmann, S. B., Mangana, J., Proulx, S. T., . . . Detmar, M. (2018). Unexpected contribution of lymphatic vessels to promotion of distant metastatic tumor spread. *Sci Adv, 4*(8), eaat4758. doi:10.1126/sciadv.aat4758

Machnik, A., Neuhofer, W., Jantsch, J., Dahlmann, A., Tammela, T., Machura, K., . . . Titze, J. (2009). Macrophages regulate salt-dependent volume and blood pressure by a vascular endothelial growth factor-C-dependent buffering mechanism. *Nat Med, 15*(5), 545-552. doi:10.1038/nm.1960

Mandriota, S. J., Jussila, L., Jeltsch, M., Compagni, A., Baetens, D., Prevo, R., . . . Pepper, M. S. (2001). Vascular endothelial growth factor-C-mediated lymphangiogenesis promotes tumour metastasis. *EMBO J, 20*(4), 672-682. doi:10.1093/emboj/20.4.672

Mishan, M. A., Ahmadiankia, N., & Bahrami, A. R. (2016). CXCR4 and CCR7: Two eligible targets in targeted cancer therapy. *Cell Biol Int, 40*(9), 955-967. doi:10.1002/cbin.10631

Montague, T. G., Cruz, J. M., Gagnon, J. A., Church, G. M., & Valen, E. (2014). CHOPCHOP: a CRISPR/Cas9 and TALEN web tool for genome editing. *Nucleic Acids Res, 42*(Web Server issue), W401-407. doi:10.1093/nar/gku410

Muto, A., Tashiro, S., Nakajima, O., Hoshino, H., Takahashi, S., Sakoda, E., . . . Igarashi, K. (2004). The transcriptional programme of antibody class switching involves the repressor Bach2. *Nature, 429*(6991), 566-571. doi:10.1038/nature02596

Nakanome, A., Brydun, A., Matsumoto, M., Ota, K., Funayama, R., Nakayama, K., . . . Igarashi, K. (2013). Bach1 is critical for the transformation of mouse embryonic fibroblasts by Ras(V12) and maintains ERK signaling. *Oncogene, 32*(27), 3231-3245. doi:10.1038/onc.2012.336

Nicenboim, J., Malkinson, G., Lupo, T., Asaf, L., Sela, Y., Mayseless, O., . . . Yaniv, K. (2015). Lymphatic vessels arise from specialized angioblasts within a venous niche. *Nature, 522*(7554), 56-61. doi:10.1038/nature14425

Ogawa, K., Sun, J., Taketani, S., Nakajima, O., Nishitani, C., Sassa, S., . . . Igarashi, K. (2001). Heme mediates derepression of Maf recognition element through direct binding to transcription repressor Bach1. *EMBO J, 20*(11), 2835-2843. doi:10.1093/emboj/20.11.2835

Oliver, G., & Alitalo, K. (2005). The lymphatic vasculature: recent progress and paradigms. *Annu Rev Cell Dev Biol, 21*, 457-483. doi:10.1146/annurev.cellbio.21.012704.132338

Oren, R., Fellus-Alyagor, L., Addadi, Y., Bochner, F., Gutman, H., Blumenreich, S., . . . Lazar, S. (2018). Whole Organ Blood and Lymphatic Vessels Imaging (WOBLI). *Sci Rep, 8*(1), 1412. doi:10.1038/s41598-018-19663-w

Ovcharenko, I., Nobrega, M. A., Loots, G. G., & Stubbs, L. (2004). ECR Browser: a tool for visualizing and accessing data from comparisons of multiple vertebrate genomes. *Nucleic Acids Res, 32*(Web Server issue), W280-286. doi:10.1093/nar/gkh355

Paduch, R. (2016). The role of lymphangiogenesis and angiogenesis in tumor metastasis. *Cell Oncol (Dordr), 39*(5), 397-410. doi:10.1007/s13402-016-0281-9

Rinderknecht, M., & Detmar, M. (2008). Tumor lymphangiogenesis and melanoma metastasis. *J Cell Physiol, 216*(2), 347-354. doi:10.1002/jcp.21494

Rossi, A., Kontarakis, Z., Gerri, C., Nolte, H., Holper, S., Kruger, M., & Stainier, D. Y. (2015). Genetic compensation induced by deleterious mutations but not gene knockdowns. *Nature, 524*(7564), 230-233. doi:10.1038/nature14580

Sainz, J., & Sata, M. (2007). CXCR4, a key modulator of vascular progenitor cells. *Arterioscler Thromb Vasc Biol, 27*(2), 263-265. doi:10.1161/01.ATV.0000256727.34148.e2

Sapoznik, S., Cohen, B., Tzuman, Y., Meir, G., Ben-Dor, S., Harmelin, A., & Neeman, M. (2009). Gonadotropin-regulated lymphangiogenesis in ovarian cancer is mediated by LEDGF-induced expression of VEGF-C. *Cancer Res, 69*(24), 9306-9314. doi:10.1158/0008-5472.CAN-09-1213

Schuermann, A., Helker, C. S., & Herzog, W. (2015). Metallothionein 2 regulates endothelial cell migration through transcriptional regulation of vegfc expression. *Angiogenesis, 18*(4), 463-475. doi:10.1007/s10456-015-9473-6

Semo, J., Nicenboim, J., & Yaniv, K. (2016). Development of the lymphatic system: new questions and paradigms. *Development, 143*(6), 924-935. doi:10.1242/dev.132431

Shajari, N., Davudian, S., Kazemi, T., Mansoori, B., Salehi, S., Khaze Shahgoli, V., . . . Baradaran, B. (2018). Silencing of BACH1 inhibits invasion and migration of prostate cancer cells by altering metastasis-related gene expression. *Artif Cells Nanomed Biotechnol, 46*(7), 1495-1504. doi:10.1080/21691401.2017.1374284

Shaw, T. J., Senterman, M. K., Dawson, K., Crane, C. A., & Vanderhyden, B. C. (2004). Characterization of intraperitoneal, orthotopic, and metastatic xenograft models of human ovarian cancer. *Mol Ther, 10*(6), 1032-1042. doi:10.1016/j.ymthe.2004.08.013

Shin, M., Male, I., Beane, T. J., Villefranc, J. A., Kok, F. O., Zhu, L. J., & Lawson, N. D. (2016). Vegfc acts through ERK to induce sprouting and differentiation of trunk lymphatic progenitors. *Development, 143*(20), 3785-3795. doi:10.1242/dev.137901

Sidwell, T., & Kallies, A. (2016). Bach2 is required for B cell and T cell memory differentiation. *Nat Immunol, 17*(7), 744-745. doi:10.1038/ni.3493

Siekmann, A. F., Standley, C., Fogarty, K. E., Wolfe, S. A., & Lawson, N. D. (2009). Chemokine signaling guides regional patterning of the first embryonic artery. *Genes Dev, 23*(19), 2272-2277. doi:10.1101/gad.1813509

Skobe, M., Hawighorst, T., Jackson, D. G., Prevo, R., Janes, L., Velasco, P., . . . Detmar, M. (2001). Induction of tumor lymphangiogenesis by VEGF-C promotes breast cancer metastasis. *Nat Med, 7*(2), 192-198. doi:10.1038/84643

Stacker, S. A., Williams, S. P., Karnezis, T., Shayan, R., Fox, S. B., & Achen, M. G. (2014). Lymphangiogenesis and lymphatic vessel remodelling in cancer. *Nat Rev Cancer, 14*(3), 159-172. doi:10.1038/nrc3677

Stimpfl, M., Schmid, B. C., Schiebel, I., Tong, D., Leodolter, S., Obermair, A., & Zeillinger, R. (1999). Expression of mucins and cytokeratins in ovarian cancer cell lines. *Cancer Lett, 145*(1-2), 133-141.

Su, J. L., Yen, C. J., Chen, P. S., Chuang, S. E., Hong, C. C., Kuo, I. H., . . . Kuo, M. L. (2007). The role of the VEGF-C/VEGFR-3 axis in cancer progression. *Br J Cancer, 96*(4), 541-545. doi:10.1038/sj.bjc.6603487

Sun, J., Hoshino, H., Takaku, K., Nakajima, O., Muto, A., Suzuki, H., . . . Igarashi, K. (2002). Hemoprotein Bach1 regulates enhancer availability of heme oxygenase-1 gene. *EMBO J, 21*(19), 5216-5224.

Tabach, Y., Brosh, R., Buganim, Y., Reiner, A., Zuk, O., Yitzhaky, A., . . . Domany, E. (2007). Wide-scale analysis of human functional transcription factor binding reveals a strong bias towards the transcription start site. *PLoS One, 2*(8), e807. doi:10.1371/journal.pone.0000807

Thiele, W., & Sleeman, J. P. (2006). Tumor-induced lymphangiogenesis: a target for cancer therapy? *J Biotechnol, 124*(1), 224-241. doi:10.1016/j.jbiotec.2006.01.007

Valastyan, S., & Weinberg, R. A. (2011). Tumor metastasis: molecular insights and evolving paradigms. *Cell, 147*(2), 275-292. doi:10.1016/j.cell.2011.09.024

Villefranc, J. A., Nicoli, S., Bentley, K., Jeltsch, M., Zarkada, G., Moore, J. C., . . . Lawson, N. D. (2013). A truncation allele in vascular endothelial growth factor c reveals distinct modes of signaling during lymphatic and vascular development. *Development, 140*(7), 1497-1506. doi:10.1242/dev.084152

Wang, S., Zhou, H., Wu, D., Ni, H., Chen, Z., Chen, C., . . . Li, X. (2019). MicroRNA let-7a regulates angiogenesis by targeting TGFBR3 mRNA. *J Cell Mol Med, 23*(1), 556-567. doi:10.1111/jcmm.13960

Warnatz, H. J., Schmidt, D., Manke, T., Piccini, I., Sultan, M., Borodina, T., . . . Yaspo, M. L. (2011). The BTB and CNC homology 1 (BACH1) target genes are involved in the oxidative stress response and in control of the cell cycle. *J Biol Chem, 286*(26), 23521-23532. doi:10.1074/jbc.M111.220178

Watari, Y., Yamamoto, Y., Brydun, A., Ishida, T., Mito, S., Yoshizumi, M., . . . Ozono, R. (2008). Ablation of the bach1 gene leads to the suppression of atherosclerosis in bach1 and apolipoprotein E double knockout mice. *Hypertens Res, 31*(4), 783-792. doi:10.1291/hypres.31.783

Wiel, C., Le Gal, K., Ibrahim, M. X., Jahangir, C. A., Kashif, M., Yao, H., . . . Bergo, M. O. (2019). BACH1 Stabilization by Antioxidants Stimulates Lung Cancer Metastasis. *Cell, 178*(2), 330-345 e322. doi:10.1016/j.cell.2019.06.005

Wissmann, C., & Detmar, M. (2006). Pathways targeting tumor lymphangiogenesis. *Clin Cancer Res, 12*(23), 6865-6868. doi:10.1158/1078-0432.CCR-06-1800

Yamazaki, H., Katsuoka, F., Motohashi, H., Engel, J. D., & Yamamoto, M. (2012). Embryonic lethality and fetal liver apoptosis in mice lacking all three small Maf proteins. *Mol Cell Biol, 32*(4), 808-816. doi:10.1128/MCB.06543-11

Yaniv, K., Isogai, S., Castranova, D., Dye, L., Hitomi, J., & Weinstein, B. M. (2006). Live imaging of lymphatic development in the zebrafish. *Nat Med, 12*(6), 711-716. doi:10.1038/nm1427

Yun, J., Frankenberger, C. A., Kuo, W. L., Boelens, M. C., Eves, E. M., Cheng, N., . . . Rosner, M. R. (2011). Signalling pathway for RKIP and Let-7 regulates and predicts metastatic breast cancer. *EMBO J, 30*(21), 4500-4514. doi:10.1038/emboj.2011.312

Zhang, S., Xu, M., Huang, J., Tang, L., Zhang, Y., Wu, J., . . . Wang, H. (2014). Heme acts through the Bach1b/Nrf2a-MafK pathway to regulate exocrine peptidase precursor genes in porphyric zebrafish. *Dis Model Mech, 7*(7), 837-845. doi:10.1242/dmm.014951

Zhou, Y., Wu, H., Zhao, M., Chang, C., & Lu, Q. (2016). The Bach Family of Transcription Factors: A Comprehensive Review. *Clin Rev Allergy Immunol, 50*(3), 345-356. doi:10.1007/s12016-016-8538-7